Lithosphere, published online on 9 January 2012 as doi:10.1130/L179.1

RESEARCH

# Hydrogeologic heterogeneity of faulted and fractured Glass Mountain bedded tuffaceous sediments and ash-fall deposits: The Crucifix site near Bishop, California

**Cynthia L. Dinwiddie[1], Kelly Keighley Bradbury[2], Ronald N. McGinnis[1], David E. Stillman[3], and David A. Ferrill[1]**
[1]DEPARTMENT OF EARTH, MATERIAL, AND PLANETARY SCIENCES, SOUTHWEST RESEARCH INSTITUTE®, SAN ANTONIO, TEXAS 78238, USA
[2]DEPARTMENT OF GEOLOGY, UTAH STATE UNIVERSITY, LOGAN, UTAH 84322, USA
[3]DEPARTMENT OF SPACE STUDIES, SOUTHWEST RESEARCH INSTITUTE, BOULDER, COLORADO 80302, USA

## ABSTRACT

Lithologic, macrostructural, microstructural, geophysical, and in situ gas permeability data from a natural exposure of highly porous, faulted and fractured tuffaceous sediments and interbedded ash-fall deposits near Bishop, California, are presented and analyzed in relation to published geologic information. This natural analog study was motivated by the need to evaluate potential length scales over which lateral flow diversion might occur above and within the nonwelded Paintbrush Tuff at Yucca Mountain, Nevada. Lateral diversion of flow in the overlying Paintbrush Tuff was previously proposed by others as a natural barrier that might protect a proposed high-level radioactive waste and spent nuclear fuel repository from percolating water. Because the length scale for capillary barrier breakthrough and leakage is decreased in the presence of subvertical structural heterogeneities, we characterized a horst-bounding fault, small-displacement normal faults within a footwall deformation zone, and secondary heterogeneities within two beds dissected by the faults. Critical deformation-related features that may influence fluid flow within bedded tuffaceous sediments include (1) permeability anisotropy imposed by steeply dipping faults and stratigraphic layering; (2) fault zone widths and styles, which are dependent on bed thickness and ash, glass, and clay content; and (3) fracture intensities and overprinting mechanisms (associated with fault deformation and vertical and nonvertical fracture orientations), which strongly influence the hydrogeologic heterogeneity of units they dissect. Microstructural analysis reveals structurally induced porosity variations at the micrometer to millimeter scale, gas permeability data show the influence of deformation on permeability at the centimeter to tens of centimeters scale, and resistivity and ground-penetrating radar data show lateral variations on the meter to tens of meters scale in horizontally bedded layers. All together, these observations and data show heterogeneity over seven orders of magnitude of length scale. Structurally enhanced porosity and permeability heterogeneities will tend to limit the length scale of lateral flow diversion, redirect flow downward, and enhance vertical fluid movement within the vadose zone.

LITHOSPHERE doi: 10.1130/L179.1

## INTRODUCTION

Integrated analyses of the lithology and structure of deformed porous, poorly consolidated to nonconsolidated rocks and sediments are important for understanding fluid-flow processes and for characterizing permeability architecture within the shallow crust (e.g., Cashman and Cashman, 2000; Rawling and Goodwin, 2003; Dinwiddie et al., 2006; Cashman et al., 2007; Evans and Bradbury, 2007; McGinnis et al., 2009). However, few studies of deformed, poorly consolidated deposits combine detailed outcrop mapping with quantitative measurements of hydrologic heterogeneity.

Predicting flow and mass transport through variably saturated deposits in the vadose zone involves a range of physical processes that depend on the texture and composition of the host lithologies, fluid type, and saturation conditions, including (1) wetting/drying hysteresis of the saturation–capillary pressure relationship; (2) wetting- and nonwetting-phase interactions and interference (Persoff and Pruess, 1993); (3) chemical exchange between liquid and gas phases; (4) gas entrapment and residual wetting-phase saturation; (5) wetting-front gravitational instability and flow fingering associated with primary heterogeneities in the geologic fabric (Hill and Parlange, 1972; Glass et al., 1988, 1989a, 1989b; Eliassi and Glass, 2002; Dinwiddie et al., 2011); (6) intra-unit fining or coarsening in the vertical direction; and (7) geologic layering, including the possible natural occurrence or geoengineered use of subhorizontal permeability or capillary barriers (Oldenburg and Pruess, 1993; Ho and Webb, 1998) that perch and laterally divert water.

Additional complexities are involved when estimating the spatial and temporal distribution of variably saturated localized preferential flow and mass transport through faulted and fractured deposits. Complicating factors include structurally superimposed secondary heterogeneities such as (1) variability in the distribution of macropores; (2) fracture density; (3) fault and fracture intersection geometry and density (Glass et al., 1995, 2003; Dragila and Weisbrod, 2004); (4) fracture apertures (Pruess and Tsang, 1990; Kwicklis et al., 1998); (5) fracture fill composition, geometry, and evolution (Dijk and Berkowitz, 1998; Pruess, 1999; Dahan et al., 1999, 2000; Salve and Oldenburg, 2001; Glass et al., 2002; Schleicher et al., 2009); (6) juxtaposition of lithostratigraphic units and/or fault lenses with marked property contrasts; (7) structurally funneled flow (Ofoegbu et al., 2001); (8) fault-zone component interactions (i.e., fault–fracture, fault–matrix, fracture–matrix, damage zone–matrix, and fault–damage zone; Caine et al., 1996), which are usually simplified in numerical models to active fracture–matrix interaction (e.g., Liu et al., 1998; Salve et al., 2003); (9) variable fracture flow modes, such as intermittent liquid bridge formation and detachment (Su et al., 1999; Ghezzehei and Or, 2005); (10) rapid film flow (Tokunaga and Wan, 1997; Tokunaga et al., 2000; Dragila and Wheatcraft, 2001; Dragila and Weisbrod, 2004);

Lithosphere, published online on 9 January 2012 as doi:10.1130/L179.1


and (11) rivulet flow or droplet sliding (Ghezzehei, 2004). These vadose zone heterogeneities and processes, which can be computationally burdensome to model, are important to environmental case studies such as transport of leached heavy metals, non-aqueous-phase liquids, and low- and high-level radioactive waste from tailings piles, leaky underground storage tanks, landfills, and geologic repositories.

High-intrinsic-permeability macropores and fractures that develop within fault deformation zones exhibit saturation-dependent intermittent behavior. High-intrinsic-permeability fault deformation zones, which can quickly transmit and drain water with percolation fluxes on the order of 10 m/yr (Pruess, 2001), act as coarse zones of subvertical capillary barriers (Glass and Nicholl, 1996; Pan et al., 2004). When liquid water above a subhorizontal capillary barrier accumulates adjacent to a subvertical fault barrier to the point of saturation, water can break through either the horizontal capillary barrier below or leak into adjacent, permeable open fractures or macropores within the fault deformation zone. At a locally saturated stage, the fault deformation zone switches from a horizontal flow barrier to a vertically transmissive conduit, such as the combined conduit–barrier system described by Caine et al. (1996). Instability-driven flow fingering, matrix and fracture heterogeneities that focus flow, and percolation fluxes on the order of 10 m/yr observed near faults together suggest that a significant volume of the unsaturated zone may be bypassed by the most rapidly moving water. Therefore, modeling highly localized and intermittent nonplug flow through unsaturated fractured rock or sediments in a volume-averaged manner is unlikely to adequately represent the nature of that flow (e.g., Pruess, 2001; Illman and Hughson, 2005).

Our work is a natural analog study with the scope of assessing hydrogeologic heterogeneities, especially those secondary heterogeneities imparted by faults and fractures on the primary fabric of the porous and permeable geologic units they dissect. This work was motivated by the need to evaluate potential length scales over which lateral diversion of flow occurs (Ross, 1990; Wilson, 1996; Webb, 1997; Pan et al., 2004) above and within the nonwelded Paintbrush Tuff (Flint et al., 2003; Manepally et al., 2007), which lies stratigraphically above the proposed high-level radioactive waste repository host horizon at Yucca Mountain, Nevada, and which is associated with localized subhorizontal permeability and capillary barriers (Flint et al., 2001; Wu et al., 2002). The nonwelded Paintbrush Tuff consists of three nonwelded ignimbrites intercalated with bedded ash-fall or reworked tuffs. The reader is referred to Manepally et al. (2007) and references therein for development of the analogy between our field site and bedded tuffs of the nonwelded Paintbrush Tuff. The Paintbrush Tuff was previously proposed as a potential natural barrier against water percolation into the geologic repository (e.g., Wu et al., 2002; Pan et al., 2004). Laterally diverted flow associated with nonwelded Paintbrush Tuff units will break through subhorizontal flow barriers in response to lateral heterogeneities, especially those produced by subvertical faults and related fracture systems that dissect the unit with regularity (Sweetkind et al., 1995; Barr et al., 1996; Engstrom and Rautman, 1996; Rautman and Engstrom, 1996a, 1996b; Eatman et al., 1997; Ho and Webb, 1998; Fabryka-Martin et al., 1998a, 1998b; Salve et al., 2003; Manepally et al., 2007). As Manepally et al. (2007) reported, mean fault spacing in the nonwelded Paintbrush Tuff is 2.23 ± 2.14 m, and mean fault dip is 69° ± 14°.

We examined volcaniclastic deposits below the basal Bishop Tuff near Bishop, California, to enhance current understanding of structural controls on permeability heterogeneity within poorly lithified, consolidated to unconsolidated sediments. At the Crucifix natural analog site, we assessed the spatial occurrence and degree of structurally induced micro- to mesoscale lithologic, hydrogeophysical, and petrophysical heterogeneities, in view of their structural geologic context (Evans and Bradbury, 2004; McGinnis et al., 2009). These structures offset and locally deform alternating subhorizontal layers of thinly bedded tuffaceous sediments and ash-fall deposits. We examined lithologic variations at the micrometer to tens of meters scales; assessed degree of cementation, postdepositional crystallization, grain-size distribution, clay content, distribution of fracture systems, and geophysical signatures; and found important lateral variations in porosity and permeability.

Observations of structural deformation features over a wide range of scales provide a basis for understanding the effects of secondarily induced lithologic change to host-rock permeability. This integrated interdisciplinary research effort is important because relatively little work has been performed to study the influence of brittle deformation on the lateral distribution of hydrologic properties in poorly lithified volcaniclastic rocks (cf. Ferrill et al., 2000; Wilson et al., 2003; Evans and Bradbury, 2004; Dinwiddie et al., 2006; McGinnis et al., 2009), and relatively few field studies have been devoted to characterizing properties that affect water flow through faulted and fractured, porous and permeable deposits (Heynekamp et al., 1999; Sigda et al., 1999; Freifeld and Oldenburg, 2000; Salve and Oldenburg, 2001; Salve et al., 2003; Sigda and Wilson, 2003).

## OBJECTIVES AND MOTIVATION

Because the hydrologic properties of bedded tuffaceous sediments and ash-fall deposits are influenced by structurally induced secondary heterogeneities at several scales, we collected multiscale data from a horst-bounding normal fault, its footwall deformation zone, and the nonfaulted protolith just beyond the footwall deformation zone to assess the characteristics and distribution of deformation features as well as the potential influence they have on permeability. Field and laboratory results address lithology-dependent, deformation-induced heterogeneities and the potential controls they have on lateral flow diversion.

## STUDY AREA

We examined and characterized the Crucifix site (so named because a memorial is placed there where two young people lost their lives), located at 37°25′5.521″N, 100°25′38.968″W, which is an exposure of poorly lithified, alternating layers of Glass Mountain–derived tuffaceous sediments and ash-fall deposits that underlie the basal Bishop Tuff in northern Owens Valley near Bishop, California (Fig. 1). The Glass Mountain volcanic complex was a precursor to the Bishop Tuff eruption and represents the first magma erupted from the Long Valley magma chamber (Metz and Mahood, 1985). Glass Mountain eruptions occurred between 2.13 and 0.79 Ma, producing high-silica rhyolite lava deposits northeast of what is now the Long Valley caldera (Metz and Mahood, 1985). Glass Mountain material was transported by Pleistocene-age glacial meltwater in the form of debris flows, hyperconcentrated flood flows (Smith, 1986), and normal stream flows, redepositing tuffaceous sediments along the valley floor (Izett et al., 1988). This fluvial system flowed sporadically and was highly variable in its flow regime (McGinnis et al., 2009). Erosion and structural uplift subsequently isolated the Crucifix site deposits as a localized topographic high (McGinnis et al., 2009).

Where the Owens River emerges from the Owens River Gorge at the southern distal extent of the 0.758 ± 0.0018 Ma (Sarna-Wojcicki et al., 2000) Bishop Tuff, the river turns sharply to the east across Owens Valley, eroding the Bishop Tuff and forming an east–west exposure known locally as Chalk Bluff. The Crucifix site is located toward the east end of Chalk Bluff on Chalk Bluff Road (Fig. 1A). At this exposure, the Bishop Tuff that once overlaid the Crucifix site deposits has been eroded by the downcutting of the Owens River. River terrace deposits consisting of unconsolidated granite cobbles

Lithosphere, published online on 9 January 2012 as doi:10.1130/L179.1


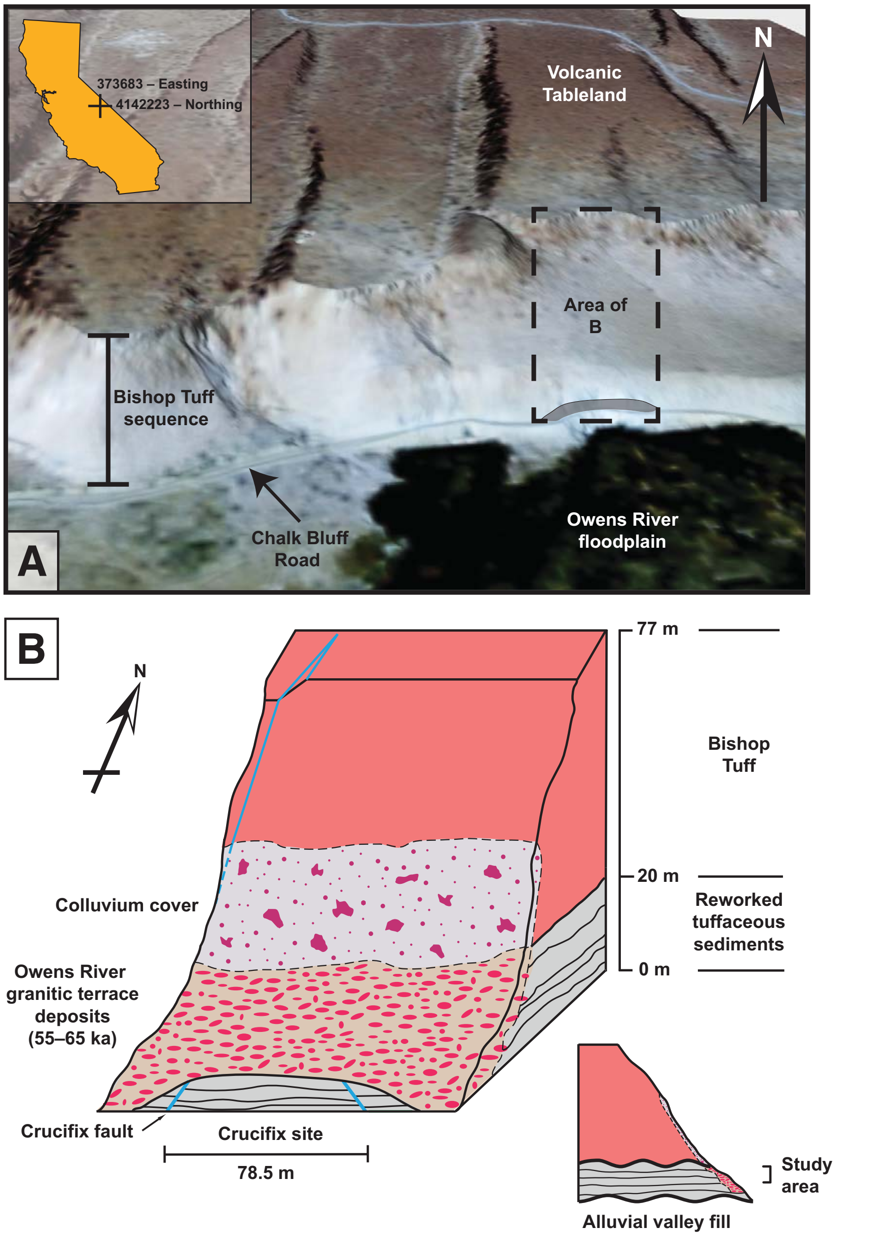


**Figure 1. Crucifix site location and geologic context. (A) View looking north across the southern boundary of the Volcanic Tableland, constructed with 1 m NAIP (National Agriculture Imagery Program) aerial imagery (U.S. Geological Survey, Earth Resources Observation and Science Center, Sioux Falls, South Dakota) draped over a 2 m LiDAR (light detection and ranging)–derived mesh (courtesy of Chevron U.S.A. Inc., a Pennsylvania company, acting through its Chevron Energy Technology Company division). See text description for height and width of Crucifix site exposure. Inset coordinates are UTM Zone 11 NAD 83. (B) Block diagram (modified from McGinnis et al. [2009], their fig. 2) depicting the Glass Mountain rhyolite-derived tuffaceous sediments and the horst-bounding faults of the Crucifix site in relation to the overlying Bishop Tuff. 1.7× vertical exaggeration.**

and gravel derived from the Sierra Nevada Mountains (Pinter et al., 1994) overlie the Crucifix site (Figs. 1B, 2A, and 3).

## PREVIOUS WORK

Previous work at the Crucifix site has focused on chronostratigraphic, lithologic, chemical, and mineralogic descriptions of the exposed ash beds (Izett, 1981; Sarna-Wojcicki et al., 1984; Izett et al., 1988), followed by characterization of fault geometry, displacements, and kinematics (Ferrill et al., 2000, 2009; Evans and Bradbury, 2004), microstructural analysis and mineralogic studies of fault-zone deformation (Evans and Bradbury, 2004), and stress history (McGinnis et al., 2009). McGinnis et al. (2009), in particular, represents a companion piece to this study because they provided the detailed structural context for the in situ permeability data in this study, with near-simultaneous field campaigns.

### Depositional History

The Crucifix site exposure consists of pumiceous and ash-rich tuffaceous sediments that exhibit varying degrees of fluvial reworking, consistent with a dominantly turbulent suspension stream system flowing into a slack-water basin or a shallow lake (B.E. Hill, 2004, personal commun.). Interbedded in these units, there are a few thin, primary ash-fall deposits (Izett et al., 1988), presumably erupted during a precaldera interval (pre–Bishop Tuff) 2.1 Ma to 790 ka. The 31-m-thick exposure (20 m above road grade and 11 m below road grade) consists of moderately to poorly sorted, fluvially reworked ash and pumice beds (Evans and Bradbury, 2004). These units are characterized by 20- to 60-cm-thick, poorly lithified consolidated to unconsolidated, horizontal to subhorizontal beds that exhibit soft sediment deformation (including burrows, load casts, and root casts) and paleosols (B.E. Hill, 2004, personal commun.). Beds are generally laterally continuous, but they occasionally pinch out or are dissected by small fluvial channels. Although the mineralogic and chemical compositions of these beds are similar to the Bishop Tuff pumice-fall deposits, the Crucifix site deposits are Glass Mountain ash-fall and sedimentary deposits derived from reworking of Glass Mountain tephra (Izett et al., 1988). Prior to structural deformation, the layered sediments of the Crucifix site would have constituted a flow divergence edifice (cf. Glass and Nicholl, 1996) at the mesoscale, potentially favorable for lateral flow diversion at bedding interfaces.

### Structural Setting and Implications for Fluid Flow

Deformation features, such as tensile, shear, and hybrid faults and fractures, impart secondary heterogeneities to the fabric of the nondeformed protolith. Faults that form in poorly lithified porous rocks may have zones of decreased pore size and reduced permeability with respect to the nondeformed host rock (e.g., Antonellini and Aydin, 1994). These zones may result from cataclastic grain-size reduction and pore collapse in deformation bands (Heynekamp et al., 1999; Wilson et al., 2003) and from clay smear (Yielding et al., 1997). Small-scale, permeability-reducing deformation features that cluster near larger faults may locally decrease

Lithosphere, published online on 9 January 2012 as doi:10.1130/L179.1



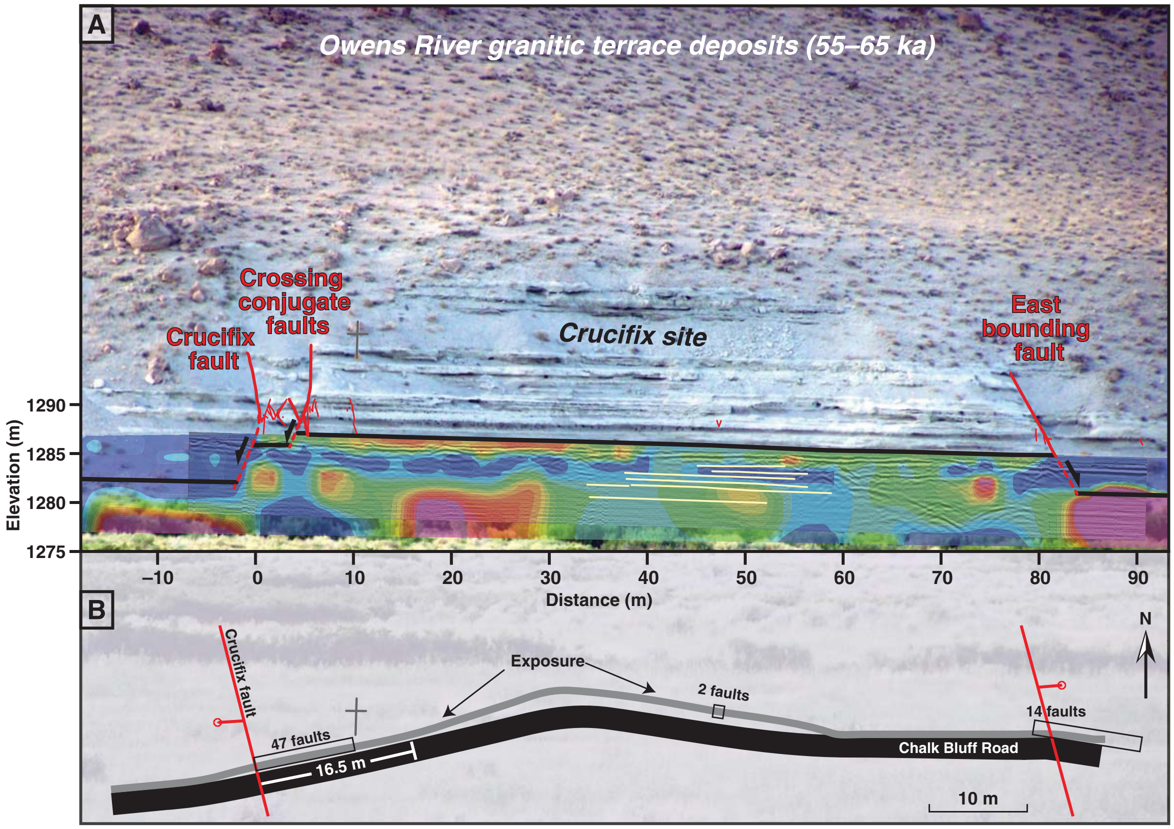


**Figure 2. Crucifix site stratigraphic, structural, and geophysical contexts. (A) Photograph of exposure draped with resistivity (see Fig. 6 for contour legend) and 200 MHz ground-penetrating radar data collected from below the surface of Chalk Bluff Road. Subhorizontal beds are indicated as mapped from the 11-m-thick exposure below the road, and surface-exposed faults are traced. (B) The exposure (gray line in map view) is 110 m long. Horst-bounding faults (red lines with ball and bar on downthrown side) and subsidiary fault clusters (boxes) illustrate asymmetric deformation across the site. We focused on the Crucifix fault and two coherent beds to a distance of 16.5 m to the east.**

flow in the fault zone by creating barriers to flow (Antonellini and Aydin, 1994; Odling et al., 2004) and thereby focus flow within the surrounding relatively nondeformed matrix. The evolution of deformation mechanisms while strain accumulates within a fault zone can cause a complex pattern of permeability structure, especially within heterogeneous sediments (Johansen et al., 2005).

Deformation observed at the Crucifix site is a product of east–west extension (McGinnis et al., 2009). The exposure trends WNW-to-ESE and ranges in height above road grade from <1 m at each end to ~20 m near its center. Small-displacement normal faults and both vertical and conjugate fractures are preserved in this 110-m-long cut bank exposure of tuffaceous sediments (Ferrill et al., 2000, 2009; McGinnis et al., 2009). Faults have visible offsets of 1 mm to >4 m and include east- and west-dipping faults that intersect and crosscut each other (McGinnis et al., 2009). The crossing conjugate style of faulting produces horst and graben structures (Ferrill et al., 2000, 2009).

McGinnis et al. (2009) observed that faults are absent from the majority of the exposure, but they are concentrated in two zones at the western and eastern ends near two oppositely dipping, horst-bounding normal faults separated by 78.5 m (Figs. 1B and 2). The horst-bounding faults account for 75% of the total fault extension in the exposure. These bounding faults correspond to the principal zones of maximum displacement, and the highest fault frequencies occur in the footwall of the western horst-bounding fault (referred to as the Crucifix fault in Evans and Bradbury [2004] and hereafter).

McGinnis et al. (2009) showed that the poorly lithified sequence at the Crucifix site underwent shear, hybrid, and up to two episodes of tensile failure as evidenced by mode I (extension fractures), mode II (shear fractures with 45°–75° dips), and hybrid (mixed mode I–mode II conjugate faults and fractures with >75° dips) structures. Overprinting structural features such as these strongly influence fluid pathways and produce permeability anisotropy in deformed strata.

Ferrill et al. (2000, 2009) described the ways in which crossing conjugate normal faulting and fracturing profoundly influence permeability anisotropy. Regardless of whether the faults have reduced or enhanced permeability, the maximum permeability direction in the deformed rock is parallel to the fault intersection line (Ferrill et al., 2009; their fig. 2; see also Pruess, 1998, their fig. 12). The faulted and fractured sediments of the Crucifix site after structural deformation constitute a flow convergence edifice (cf. Glass and Nicholl, 1996) at the mesoscale, which limits the length scale of lateral flow diversion.

## CHARACTERISTICS OF TUFFACEOUS SEDIMENTS

### Field and Laboratory Methods

Building on previous fault and fracture characterization (Ferrill et al., 2000, 2009; Evans and Bradbury, 2004; McGinnis et al., 2009), we used an integrated approach whereby lithologic,

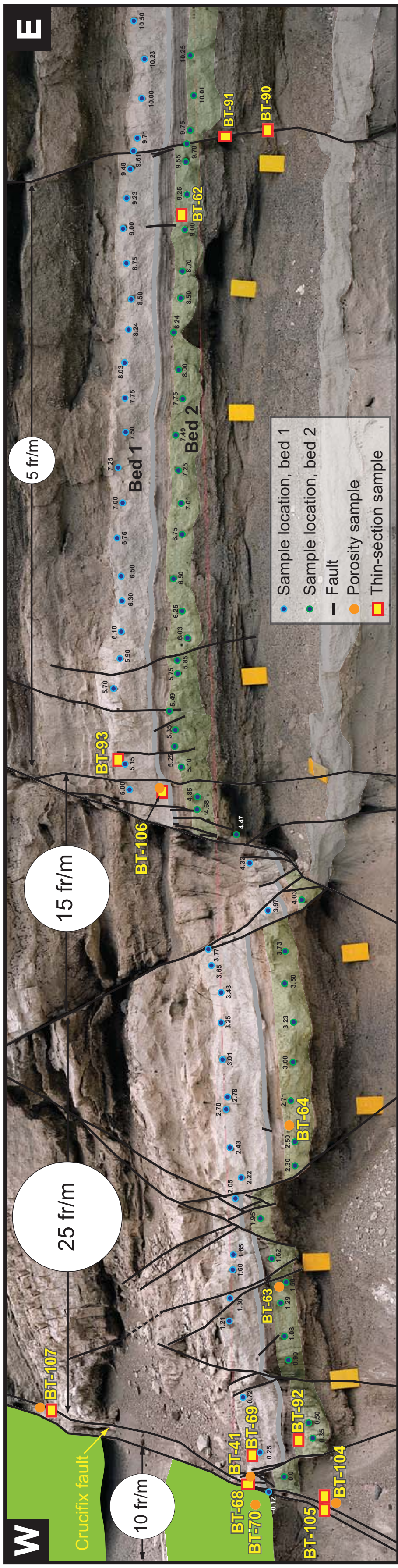


**Figure 3.** Photomosaic of Crucifix fault and 10.5 m of footwall block (modified from McGinnis et al., 2009, their fig. 8) with beds 1 and 2, and grain size, permeability, and lithologic sample locations identified. Fracture intensity for discrete regions is given as the number of fractures per meter (fr/m).

geophysical, and microstructural data were collected to provide additional context for permeability measurements within tuffaceous beds at the Crucifix site. Grain-size analysis, compositional and microstructural thin-section studies, specific gravity measurements, and X-ray diffraction (XRD) analyses were conducted along two transects extending perpendicular to the Crucifix fault eastward to 10.5 m into the footwall block (Fig. 3). Gas permeability surveys were conducted along these same transects eastward to 16.5 m into the footwall block (Fig. 2B). Finally, we calculated areal fracture density around each gas permeability test hole based upon circular fracture survey data that McGinnis et al. (2009) acquired.

Lithologic and gas permeability data collection focused on two relatively well-consolidated beds (hereafter bed 1 and bed 2) that were selected for study because of their lateral consistency in thickness and texture. Bed 1, which is the ash bed called Glass Mountain-D by Izett (1981, p. 10,217), is white to light gray, averages 12.5 cm thick, and is interpreted to be either a primary ash-fall deposit or a slack-water ash-fall deposit because it is massive and exhibits no internal bedding (B.E. Hill, 2004, personal commun.). Bed 2 is greenish gray to yellowish-greenish gray, averages 18.8 cm thick, and is interpreted to be a reworked pumiceous tephra-fall deposit with possible development of a paleosol (B.E. Hill, 2004, personal commun.). Lithologic and gas permeability data were also collected within the main trace of the Crucifix fault and subsidiary fault zones.

Near-surface geophysical surveys using ground-penetrating radar and multielectrode resistivity were conducted along the surface of Chalk Bluff Road (at an orientation near-perpendicular to fault strike) to extend our site characterization into the subsurface, illuminate subsurface offsets on the two horst-bounding faults, and extend assessment of lateral heterogeneities to the tens of meters scale (Fig. 2A). Subsurface displacements on meter-scale faults may be estimated from vertical offsets of contoured patterns within resistivity data, but they commonly cannot be determined from radar data. Discontinuities in near-horizontal geologic bedding can be inferred from offset reflectors in high-lateral-resolution radargrams, but these same discontinuities are below the lateral resolution of resistivity data inversions. Used together, these two geophysical data types provide more information than either would alone. Precise knowledge of fault locations in the exposure enables us to determine the resistivity signature of faults with meter-scale displacements and the radar signature of bedding discontinuities, potentially attributable to (1) faults with submeter- to

Lithosphere, published online on 9 January 2012 as doi:10.1130/L179.1


meter-scale displacements, (2) small fluvial channels known to dissect some beds within the exposure, or (3) bedding pinch-outs.

Variation of electrical resistivity within a relatively homogeneous geologic bed in the vadose zone is commonly related to moisture content, with low-resistivity (high-conductivity) zones generally related to greater moisture content in otherwise uniform rock or sediment (Roberts and Lin, 1997; Roberts, 2002). Multiphase fluid saturation may be inferred from the spatially variable electrical resistivity and radar attenuation of rocks or sediments. Water causes attenuation at radar frequencies via both direct-current electrical conductivity and dielectric relaxations caused by adsorbed and bulk liquid water (e.g., Stillman and Olhoeft, 2008). Also, radar reflections can be caused by moisture content variability because liquid water has an order-of-magnitude higher dielectric permittivity than dry rock or sediment (e.g., Parkhomenko, 1971).

With the exception of these geophysical methods, the methods we employed at the Crucifix site and summarize next were also used and described in previous studies (Evans and Bradbury, 2004; Dinwiddie et al., 2006; McGinnis et al., 2009) to which the reader is referred for additional detail, if desired.

### Geologic Mapping and Fracture Data

To assess lithologic and structural relationships within the tuffaceous sediments and ash-fall deposits and to correlate these relationships with locations where in situ permeability data were collected, 1:25 scale outcrop mapping was completed within beds 1 and 2 in the footwall block of the Crucifix fault (Fig. 3). The Crucifix fault trace represents the datum for detailed mapping, with transect lines oriented perpendicular to the main trace of the fault and extending 10.5 m to the east into the footwall block. Mapping at the centimeter scale highlights several of the features presented in McGinnis et al. (2009) and delineates variations in lithologic properties that may influence permeability.

Areal fracture density (cm/cm$^2$) data provide information about the intensity and distribution of fracturing throughout the exposure. Areal fracture densities for more than 3000 vertical and conjugate fractures (McGinnis et al., 2009) were calculated by dividing total fracture trace length within a 25-cm-diameter circle centered on each permeability test hole by measurement area within the 25-cm-diameter circle. A circle was selected as the most appropriate two-dimensional shape from which to measure fractures that may intersect the averaging volume of the permeability measurement (cf. Molz et al., 2003). Permeability test holes were spaced approximately every 25 cm, so a 25-cm-diameter circle provided nearly complete coverage of fractures occurring within each bed, while minimizing the potential for fractures to be double-counted.

### Geophysical Mapping

Resistivity surveys measure injected current through transmitting electrodes and potential difference between two receiving electrodes. Multielectrode resistivity profiling along Chalk Bluff Road was performed using an IRIS Syscal Pro 10-channel resistivity meter. Two multielectrode resistivity surveys (dipole–dipole array using 1 m spacings and 96 electrodes) were collected ~1–2 m in front of the exposure—one survey, including that from the eastern horst-bounding fault, was performed on 25 July 2006, and the other survey, including that from the Crucifix fault, was performed on 4 June 2007. The two data sets were merged into a single profile, and an inverse model of the combined resistivity data was run using RES2DINV to produce a detailed map of the electrical properties (i.e., current, voltage, and resistivity) of the subsurface (Loke and Barker, 1996; Loke, 2010).

Ground-penetrating radar data were gathered along the same geophysical transect in 2006 and 2007 using a Sensors and Software pulseEKKO PRO geological ground-penetrating radar system with 400 V low-frequency transmitter and antennas or high-frequency transducers spanning the frequency range from 25 to 1000 MHz. We document the 200 MHz radargram with 10 cm lateral resolution and the 250 MHz radargram with 5 cm lateral resolution here. Radar wave velocity in the ground, calculated as 0.11 m/ns from a common midpoint survey and semblance analysis (consistent with the real part of the dielectric permittivity equaling ~7—the expected value for partially saturated rock), was used to convert two-way traveltime to depth. Ground-penetrating radar data were minimally processed with Ekko_view Deluxe version 1, release 4 software, including dewow filtering and SEC2 gaining. The geophysical data were topographically enhanced using elevation data measured along Chalk Bluff Road with a Trimble® real-time kinematic differential global positioning system system.

### Grain Size, Sorting, and Weight Percent Fines Analyses

Grain-size samples were collected from exposed material at the proximal end of permeability test holes in beds 1 and 2 and from locations within the fault core, which consisted of lenses of this bed material and clay gouge. Samples were collected for standard sieve analysis (cf. Boggs, 1995) to track centimeter-scale changes in lithologic properties throughout each bed, such as mean grain size, degree of sorting, and weight percent fines. Grain-size sampling of bed 1 extended from the Crucifix fault to 10.5 m to the east, and 37 samples were collected. Bed 2 sampling extended from the Crucifix fault to 10.25 m to the east, and 38 samples were collected. The total mass collected averaged 76 g per sample for bed 1 and 112 g per sample for bed 2, with the difference due primarily to bed 1 being generally thinner, more ash rich, and slightly more cohesive than bed 2.

Grain-size samples were dry sieved and hand shaken to (1) reduce disruption of the ash particles; (2) avoid abrasion of the pumice fragments by overshaking (a method selected to preserve delicate volcaniclastics); and (3) include the low-density pumice and glass shards and fine-grained fraction that might have otherwise separated out of the fines using liquid settling methods. Standard granulometry methods (e.g., Balsillie et al., 2002) were used to analyze grain size and formulate cumulative probability curves. Weight percent fines data were also calculated from the original grain size data. We selected a cutoff grain size of 0.0625 mm (or 4φ, where the grain size measure $\varphi = -\log_2[d/d_0]$ and $d_0$ = 1 mm) for the weight percent of fines of the total sample because it represents the upper size limit for ash deposits that Fisher (1961, 1966) defined for pyroclastic sequences. Thus, the weight percent of fines is a proxy for ash content.

### Microstructural Analyses

Thin-section preparation of friable sediments and poorly lithified rock is challenging, and the methods we used are described in Evans and Bradbury (2004, Appendix). Microstructural analyses were performed on thin sections using a standard transmitted-light petrographic microscope to evaluate textural and compositional variations between deformed and relatively undeformed samples. Fifteen samples for thin sections were collected from beds 1 and 2, and 13 samples were collected from the Crucifix fault core or subsidiary faults within the footwall deformation zone. All samples were impregnated with blue-dyed epoxy and examined using standard optical petrography techniques; ten of these samples were collected during a previous study by Evans and Bradbury (2004). Samples collected from deformed sediments were examined to identify specific deformation features and deduce the potential influence of microstructural features on porosity and permeability.

Twelve thin sections (grain mounts) were analyzed using a modified point-count method (cf. Schmid, 1981; Boggs, 1992) to express the relative lithologic and mineralogic composition. Individual counts were made every 0.5 mm to form a 150-point grid over the slide area. The composition was recorded at each point with subcategories designated for crystals and crystal fragments (predominately quartz and feldspar), pumice and glassy fragments, lithics, fine-grained matrix, and alteration products that include iron oxides, carbonates, and zeolites. Individual point counts were recorded as a percentage of the total count. To compare weight percent fines obtained from grain-size analyses to thin-section point count data, we used the total percentage of fine-grained matrix from point counting as an analog to the weight percent fines.

### Compositional Analyses

Very fine-grained particles and alteration products, including abundant glassy material within the reworked tuffaceous sediments, are difficult to identify at the thin-section scale. Therefore, as a supplemental technique, we use XRD analyses to determine mineralogical composition of whole-rock samples. Representative samples were collected within beds 1 and 2 and from the Crucifix fault and subsidiary faults. Twenty-one whole-rock powdered samples were analyzed using a Norelco model 12045 (Philips Electronic Instruments) system running at 35 kV, 15 mA with copper anode tubing from 2° to 60° using 2° step angles. This work expands on previous compositional analyses of Crucifix site samples by Evans and Bradbury (2004).

### Porosity and Density Analyses

We used a specific gravity measurement technique based upon Archimedes' principle and the assumption that the solid constituents had mineral and glass fractions equivalent to those reported by Hildreth (1979) and Wilson and Hildreth (1998) for the nonwelded Bishop Tuff (see Evans and Bradbury [2004, Appendix] for additional detail). We used a modified jolly balance and the specific gravity technique to calculate total porosity of two representative whole-rock samples from bed 1, three samples from bed 2, and four samples from the Crucifix fault core.

### Small Drill-Hole Minipermeameter Survey

We used a small drill-hole minipermeameter probe (Dinwiddie et al., 2003; Dinwiddie, 2005) to measure the gas permeability of the deposits. Dinwiddie et al. (2006) used the same approach to assess permeability heterogeneity within a fault zone in the nonwelded basal Bishop Tuff. Use of this in situ method (1) eliminates the need to extract fragile samples for laboratory analysis and (2) minimizes effects of weathering on the measured permeability value by sampling rock that is not directly exposed to the atmosphere (we cannot be certain we are sampling nonweathered material, however). The small drill-hole minipermeameter probe is inserted into a 10-cm-long, 1.8-cm-diameter hole until the faceplate contacts the conical end of the drill hole. An annular rubber tip seal packer is then axially compressed, causing the seal to radially expand like a packer against the sides of the drill hole. The packer seals the probe to the distal end of the drill hole while isolating the injection zone through which pressurized nitrogen gas is introduced to the porous medium. Pressure within the sealed-off region is maintained above atmospheric, so that nitrogen gas enters the porous medium, flows around the tip seal packer, and exits to the surface at ambient pressure. After steady-state conditions are achieved, several pressure and flow-rate data pairs are recorded. The pressure transducer and three flow meters were each calibrated to National Institute of Standards and Technology–traceable standards at the beginning and end of field campaigns. In the event of instrument drift, calibration curves were used to correct pressure or flow-rate data. A portable, homogeneous ceramic check source was also used to calibrate the small drill-hole minipermeameter system daily in the field. Pressure and flow-rate data pairs from each location were analyzed for the presence of high-velocity flow effects, and corrections were made if warranted. In the arid, windy environment of the Crucifix site exposure, water saturation is naturally low; thus, the use of effective gas permeability data as a surrogate for intrinsic permeability is thought to be appropriate (i.e., the relative permeability for a gas is approximately unity).

The effective gas permeability of the porous medium surrounding the drill hole was calculated with a semi-analytical inverse solution (Dinwiddie et al., 2003; Dinwiddie, 2005) given the measured injection pressure and flow rate, a numerically determined geometrical factor describing the flow system, and the standard assumption of local homogeneity within the averaging volume. The complete permeability data set for the Crucifix site was collected over three field campaigns. Initially, the permeability sampling intervals were ~0.5 m, and the survey terminated at a distance of ~10.5 m from the Crucifix fault, but measurement density was ultimately increased to a sampling interval of ~0.25 m, and the survey line was extended to a distance of 16.5 m. Permeability test holes were drilled approximately perpendicular to the local outcrop face. Permeability was determined for (1) 67 locations in bed 1, including three fault locations; (2) 76 locations in bed 2, including three fault locations; and (3) four locations in the Crucifix fault core. Unlike Dinwiddie et al. (2006), we were unable to measure permeability of the nondeformed host rock because vertical, mode I fractures are present throughout the exposure (McGinnis et al., 2009), which influence the secondary permeability of the measured volume.

Permeability and grain-size data are sparse in the 2 m of the footwall immediately adjacent to the Crucifix fault and near a crossing conjugate fault system (Fig. 3). Most of the strain was localized here, which theoretically should strongly affect the flow field and fluid rock interactions. These areas experienced more intense deformation than the rest of the exposure (Ferrill et al., 2000, 2009), which likely weakened the rock and accelerated weathering. Poor rock quality in some locations prevented an adequate tip seal around the minipermeameter, thereby limiting data acquisition. Data scarcity near the crossing conjugate faults was not attributable to tip seal issues, but was instead a result of conjugate fault dilation, which allowed very small widths of the target beds to descend into the larger opening (Fig. 3)—there is less target bed width than total measured transect width as a result.

## RESULTS

### Fault and Fracture Summary

The Crucifix fault is a north–south–striking, west-dipping normal fault with 3.77 m of fault-parallel displacement (McGinnis et al., 2009), and it is characterized by a 20-cm-thick central core consisting of volcaniclastic sediments and clay gouge. The central fault core is multilayered and bounded by two discrete 1- to 3-mm-thick slip surfaces coated with white calcite and/or clay (Fig. 4). The fault core thickness is variable, ranging from 1.5 to 30 cm vertically (Evans and Bradbury, 2004). Cataclasis and clay smearing processes have contributed to an anastomosing, comminuted, fine-grained fault gouge surrounding multiple continuous to discontinuous lenses of host-rock material and/or clay gouge that were locally dragged up to 1 m or entrained in the fault zone parallel to the slip direction (Fig. 4). The Crucifix fault core is heterogeneous and variably filled with calcite, coated with clay, or consists of fine-grained gouge mixed with glassy fragments or pumice clasts.

Deformation is pervasive throughout the domain between the Crucifix fault and the


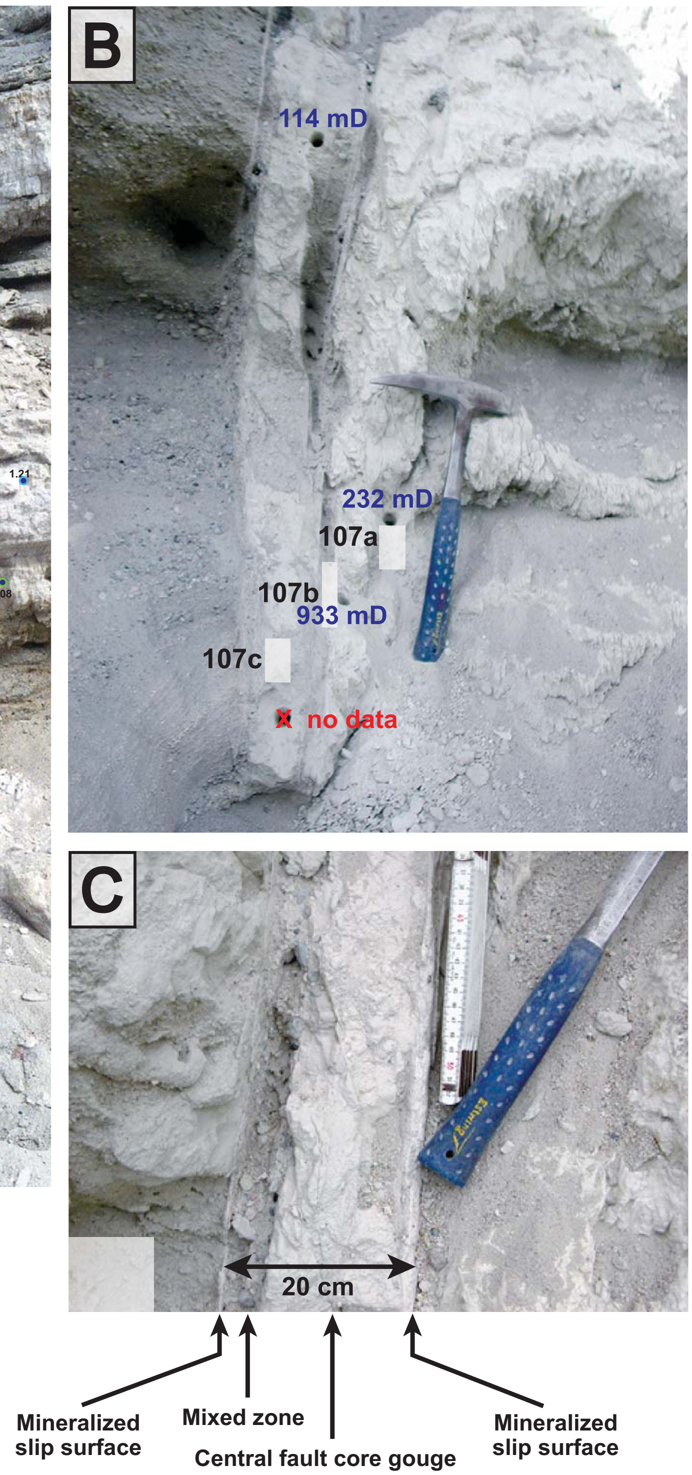


**Figure 4. (A) Crucifix fault (see Fig. 3 for context). (B) Sample collection locations for three thin sections and permeabilities measured in three drill holes. (C) The fault core includes multiple layers, and its properties change vertically and horizontally. Beds of reworked volcaniclastics are entrained within the mixed outer zones of the Crucifix fault core, whereas clay gouge makes up the central zone. The millimeter-thick bounding slip surfaces of the fault are mineralized by calcite, suggesting fluid-flow interactions along the fault (after Evans and Bradbury, 2004, their fig. 7B).**

parallel fault 4 m to the east, and it includes abundant small-displacement conjugate normal faults and an 8° bedding dip to the west (Figs. 3 and 4; Ferrill et al., 2009). Little deformation is observed west and east of this pair of faults (Evans and Bradbury, 2004; Ferrill et al., 2009; McGinnis et al., 2009), and we interpret the synthetically west-dipping panel between these west-dipping faults (Fig. 3) as a relay ramp (Ferrill et al., 1999, 2005; Ferrill and Morris, 2001). Similar relay ramps are abundant in the moderately welded Bishop Tuff across the Volcanic Tableland surface, where they are exposed in three dimensions (Ferrill et al., 1999; Ferrill and Morris, 2001). The footwall of the Crucifix fault exhibits a nonuniform fault and fracture distribution (McGinnis et al., 2009, their figs. 8A and 8B), extending eastward ~10 m, through the relay ramp and into the footwall. Of the 47 faults measured along a scan line within the footwall block of the Crucifix fault (Fig. 2B), 25 surfaces were mapped within a 2-m-wide zone immediately east and adjacent to the Crucifix fault trace (Fig. 3). The Crucifix fault footwall damage zone is characterized by small-displacement antithetic, synthetic, and en echelon faults that are moderately to steeply dipping (Evans and Bradbury, 2004; McGinnis et al., 2009). Beds adjacent to these smaller faults are offset by numerous centimeter-scale slip surfaces. Mineralization surfaces up to several millimeters thick composed of calcite and/or silica are observed along some of the smaller slip surfaces (Evans and Bradbury, 2004). Associated fractures are typically open with 1–5 mm mechanical apertures and vertical to steeply east or west dipping. The hanging wall, however, has no associated faults and only centimeter-scale subvertical fractures immediately west of the fault (McGinnis et al., 2009).

The geometry of faults at the Crucifix site, including local fault core thickness, is dependent on the scale of displacement and the grain size and competence of the beds through which the faults cut (e.g., McGinnis et al., 2009, their fig. 5). The intrinsic permeability of the fault core(s) is expected to be low as a result of (1) mineralization processes, (2) grain comminution and pore collapse in coarse-grained material, and (3) neomineralized clay growth and clay smear processes in fine-grained material.

Two distinctive fracture patterns are observed at the Crucifix site: (1) vertical fractures dominate the less-deformed areas of the exposure and (2) oppositely dipping, steep but nonvertical conjugate fractures dominate in highly faulted areas (McGinnis et al., 2009). The greatest concentration of conjugate fractures occurs (1) in a highly faulted section between the Crucifix fault at 0 m and 10 m into the footwall and (2) in a nonfaulted section located 14.5–16.5 m east of the Crucifix fault (Fig. 5). The areal fracture density data also show that pervasive conjugate fracture systems associated with the Crucifix fault extend into the footwall block for ~6 m, with minor variation dependent on the bed lithology.

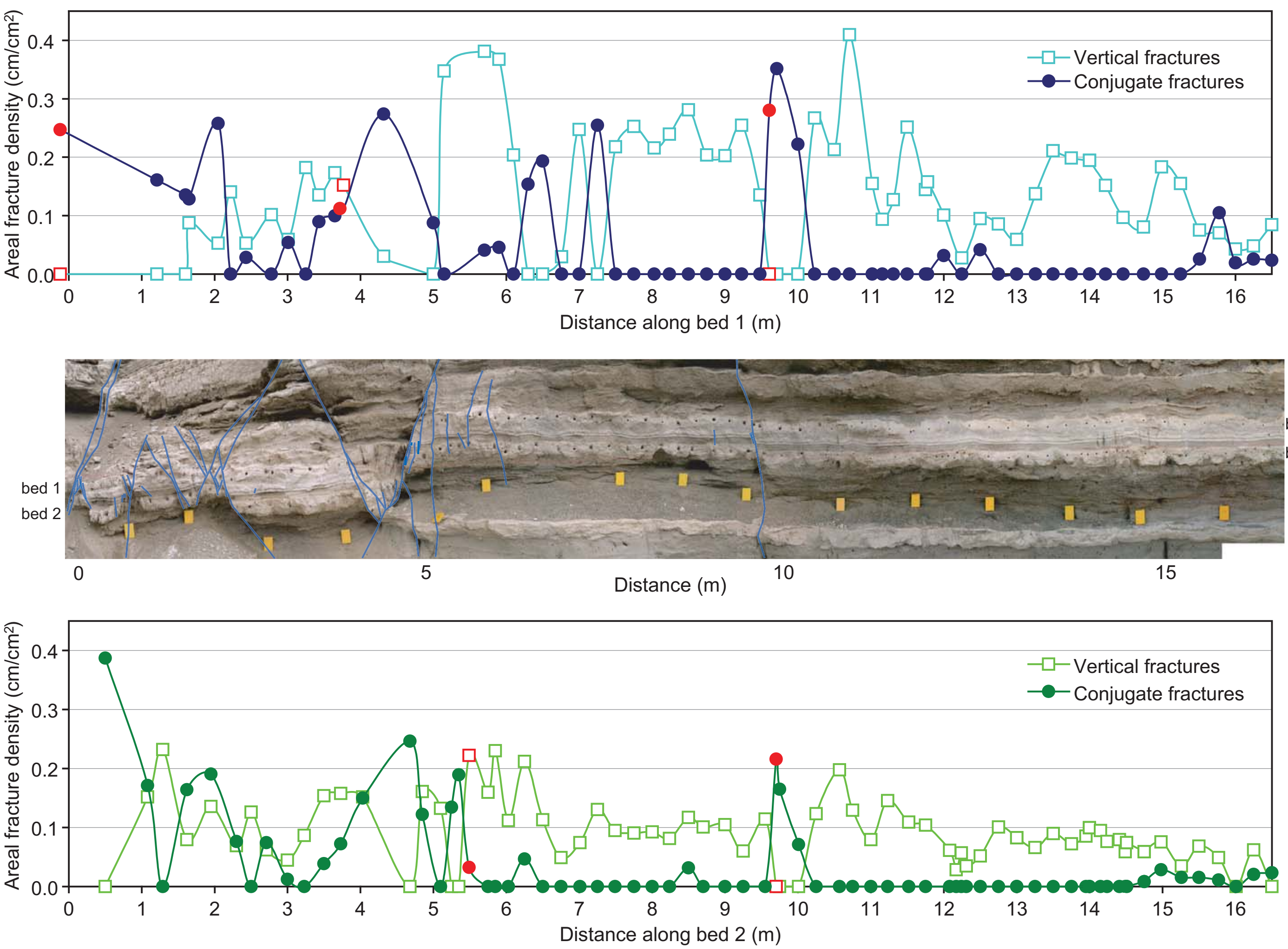


**Figure 5. Areal fracture density within 25-cm-diameter circles centered around permeability test holes, as calculated from the trace length and fracture set data of McGinnis et al. (2009). Red points denote drill holes intersecting fault zones.**

Lithosphere, published online on 9 January 2012 as doi:10.1130/L179.1


Beyond this distance, conjugate fracturing tapers off significantly, and vertical fractures dominate.

McGinnis et al. (2009) showed that the Crucifix site has a history of deformation that includes cataclastic shear deformation, extension fracturing, variations in fault-zone architecture-controlled small-displacement faults and fractures near larger-displacement faults, and overprinting of different failure modes and deformation mechanisms. Overprinting associated with episodic (or cyclic) deformation can cause the temporal evolution of permeability characteristics (Johansen et al., 2005). The stratigraphy and structural context of two lithologically distinct beds and locations where permeability, grain size, and fracture data were collected are highlighted in Figure 3. Also shown are fault traces from McGinnis et al. (2009) with offsets ranging from 2 cm to several meters and with fault core thicknesses ranging from <1 cm to 30 cm. Lithologic properties for beds 1 and 2 and fault systems are summarized in Table 1.

## Mesoscale Heterogeneity Insights from Geophysical Data

Our geophysical results are sensitive to the prevailing moisture status of the geologic units, and although our data were not all collected during the same year, it is likely that we sampled similar summer-season moisture conditions during both field campaigns. Mean annual precipitation in Bishop, California, is 135 mm, and only 8% of annual precipitation on average is accumulated during summer months June through August (Western Regional Climate Center, 2011). In July 2006, we collected 96 m of 25–200 MHz radar data spanning the horst (e.g., Fig. 2A radargram) and 96 m of multielectrode resistivity data spanning the eastern horst-bounding fault (Fig. 6). In June 2007, we collected 117 m of 250–1000 MHz radar data spanning the horst (e.g., Fig. 6 radargram) and 96 m of multielectrode resistivity data spanning the western horst-bounding (Crucifix) fault (Fig. 6). The two resistivity data sets, which had 3 m of electrode overlap from 37.4 to 40.4 m along the merged profile, were inverted with a small region subject to interpolation (Fig. 6). The year 2006 was average in terms of total precipitation, and 2007 had less than average precipitation, totaling only 47 mm. July 2006 was a relatively wet month (6.6 mm precipitation) during a record-breaking heat wave and monsoon season, preceded by two dry months in May (2 mm) and June (1.5 mm). No precipitation was recorded in either May or June 2007, with March being very dry (0.8 mm) and April (4.3 mm) being relatively wet (Western Regional Climate Center, 2011).

Multielectrode resistivity data were collected at this site in two sections separated in time by ~10.5 mo. The dynamic range of the two data sets is similar (Fig. 6): both data sets were collected from an arid site during the driest season, and most of the precipitation that fell during July 2006 should have been lost to evaporation and runoff rather than have transitioned to net infiltration. This suggests that the data are useful for understanding relative electrical heterogeneities across both surveys. While the resistivity signature of the Crucifix site will fluctuate with respect to recharge events, the most significant recharge events typically occur during the winter season. Radar signal attenuation patterns from 2006 and 2007 that are consistent with expected direct-current conductivity losses also support the interpretation that the jointly inverted resistivity profile is representative of an average dry season condition.

Resistivity data indicate the near-surface geology of the Crucifix Site is horizontally layered, but vertically offset contouring patterns illustrate complex lateral heterogeneity (Fig. 6). Purple- to

TABLE 1. ROCK PROPERTIES OF CRUCIFIX SITE DEPOSITS AND FAULT ELEMENTS

| Unit/feature identifier | Unit/feature description* | Lithologic characteristics |
|---|---|---|
| Bed 1 | Upper bed | • White to light gray, ash-rich fallout deposit, either a primary or slack-water deposit<br>• Thinly bedded (12.5 cm average thickness)<br>• Density: 0.92 g/cm$^3$<br>• Porosity: 0.63<br>• Poorly sorted<br>• Grain size: 78 wt% fines (≤0.0625 mm) on average; geometric mean grain size: 0.15 mm<br>• Average composition: 21.8 wt% crystals (quartz, feldspar); 0.7 wt% lithics; 13.3 wt% glassy fragments and pumice; 59.8 wt% fine-grained matrix; 4.4 wt% miscellaneous† <br>• Permeability (geometric mean): 342 mD |
| Bed 2 | Lower bed | • Greenish gray to yellowish-greenish gray, reworked pumiceous tephra-fall deposit<br>• Thinly bedded (18.8 cm average thickness)<br>• Density: 1.21 g/cm$^3$<br>• Porosity: 0.52<br>• Moderately to poorly sorted<br>• Grain size: 19 wt% fines (≤0.0625 mm) on average; geometric mean grain size: 0.40 mm<br>• Average composition: 32.0 wt% crystals (quartz, feldspar); 10.0 wt% lithics; 20.0 wt% glassy fragments and pumice; 36.7 wt% fine-grained matrix; 1.3 wt% miscellaneous†<br>• Permeability (geometric mean): 254 mD |
| CFa | Crucifix fault core | • Fault core gouge composed of variable layers of entrained bedding and clay<br>• Density: 0.76–1.77 g/cm$^3$<br>• Porosity: 0.29–0.70<br>• Grain size: 51 wt% fines (≤0.0625 mm)<br>• Average composition: 11.3 wt% crystals (quartz, feldspar); 2.4 wt% lithics; 13.6 wt% glassy fragments and pumice; 69.9 wt% fine-grained matrix; 2.8 wt% miscellaneous†<br>• Permeability: 114–933 mD |
| CFb | Subsidiary faults | • Grain size: 58 wt% fines (≤0.0625 mm)<br>• Average composition: 20.3 wt% crystals (quartz, feldspar); 1.7 wt% lithics; 26.0 wt% glassy fragments and pumice; 51.3 wt% fine-grained matrix; 0.7 wt% miscellaneous†<br>• Permeability: 40–940 mD |

*Refer to Figure 3 for location.
†Iron oxides and alteration products.

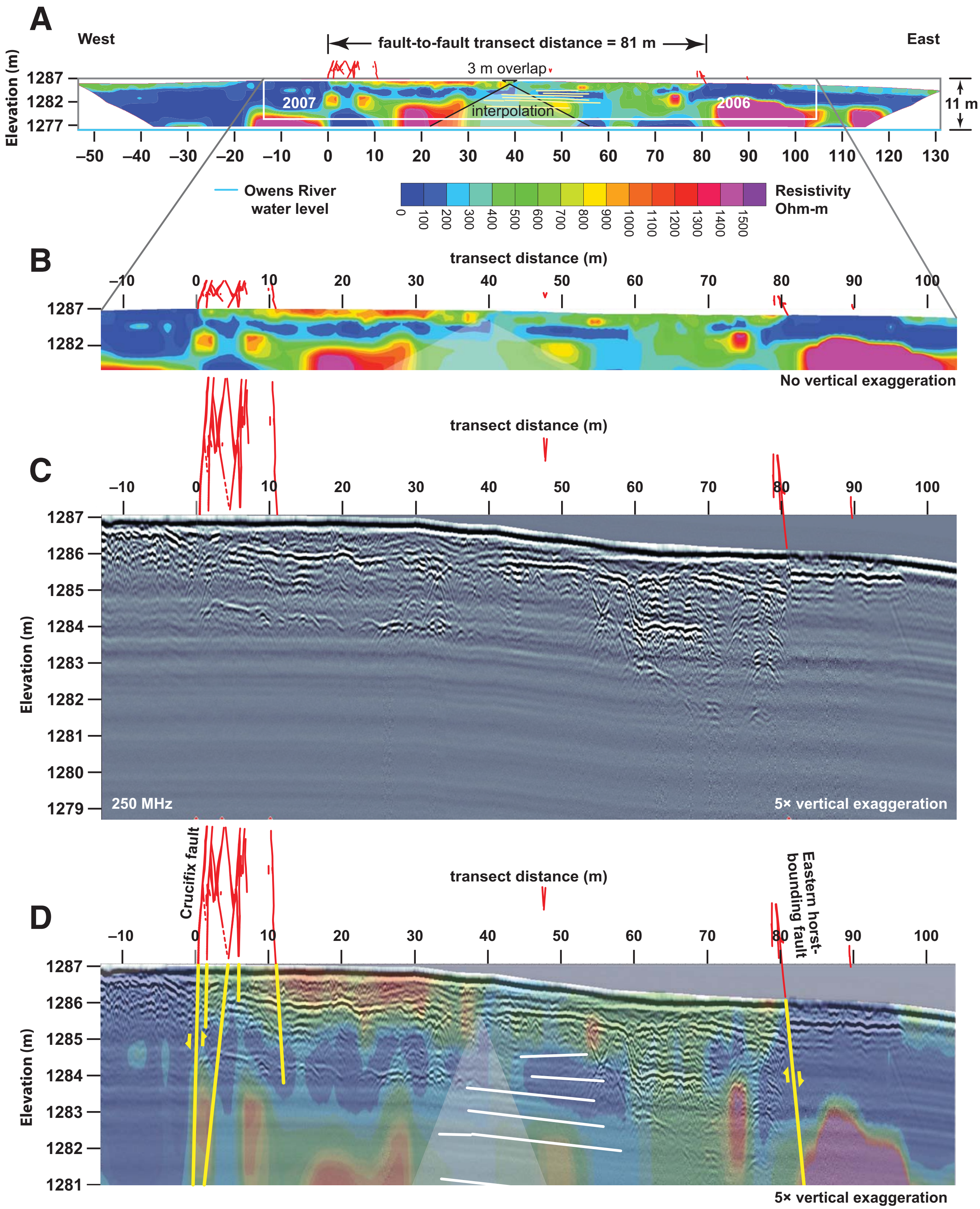


**Figure 6.** Geophysical data and their interpretation relative to known through-going fault locations/dips and mapped bedding interfaces. All data are for the vadose zone above the adjacent Owens River. (A) Resistivity profile along Chalk Bluff Road; horizontal distances in meters with datum at the Crucifix fault; no vertical exaggeration. (B) Section of resistivity profile coincident with radar profile; no vertical exaggeration. (C) 250 MHz uninterpreted ground-penetrating radar profile with 5× vertical exaggeration. (D) Interpreted patina plot of complementary radar and resistivity profiles with 5× vertical exaggeration. Tilted beds and bedding disruptions potentially attributable to nonverifiable subsurface faults or fluvial channels are evident, but not formally interpreted.

Lithosphere, published online on 9 January 2012 as doi:10.1130/L179.1



yellow-colored zones indicate resistivity values from 800 to 1500 ohm-m and are interpreted to represent relatively dry regions associated with larger grain sizes, macropores, and high-intrinsic-permeability fault zone deformation, including secondary open-fracture porosity. Blue- to green-colored zones range from 0 to 799 ohm-m and are interpreted to represent relatively moist zones associated with smaller grain sizes where intrinsic permeability is low but relative permeability to water is high. The geophysical transect on Chalk Bluff Road was curved such that the transect distance between the two horst-bounding faults was 81 m (not to be confused with the true separation distance between these faults of 78.5 m). Large-scale lateral resistivity symmetry across this horst is evident despite data collection having taken place during two years with mildly different precipitation histories.

High-resistivity zones occur in the footwall between the Crucifix fault and the parallel crossing conjugate fault, and between the parallel crossing conjugate fault and the small-displacement fault located ~10 m along the geophysics transect, especially at elevations from 1284–1281 m (Fig. 6). Above this level, at an elevation between 1285 and 1284 m, there is a very broad, laterally continuous conductive unit that nearly extends to 60 m along transect. This conductive zone significantly attenuates the radar signal such that few features are observed below this level in radargrams.

Geologic units immediately surrounding the eastern bounding fault, except at the very near surface, are conductive to an elevation of 1283 m (Fig. 6). However, west of the eastern horst-bounding fault, there is a very broad zone from 50 to 80 m along transect where moderately high to high resistivities dominate (Fig. 6). The highest resistivities in this broad zone are laterally congruous with bedding disruptions in radargrams (Fig. 5). Also consistent with the moderately high to high resistivities of this zone are the deepest radar signal penetrations at the site.

## Grain Size, Sorting, and Weight Percent Fines

Grain-size data provide information about depositional and deformational processes at the centimeter scale. The data are highly skewed toward smaller grain sizes (Fig. 7A); therefore, the geometric mean is the appropriate measure of central tendency for this parameter. On average, the primary or slack-water deposited ash-fall material of bed 1 has a 0.15 mm grain size, while the reworked pumiceous tephra of bed 2 has a 0.40 mm grain size. Excursions from average behavior that tend to occur at similar distances from the western horst-bounding fault are attributed to a combination of the random occurrence of large pumice clasts and the potentially nonrandom occurrence of more agglutinated particles near the Crucifix fault. The particles from this location remained strongly agglutinated upon hand-shaking and sieving, which may indicate

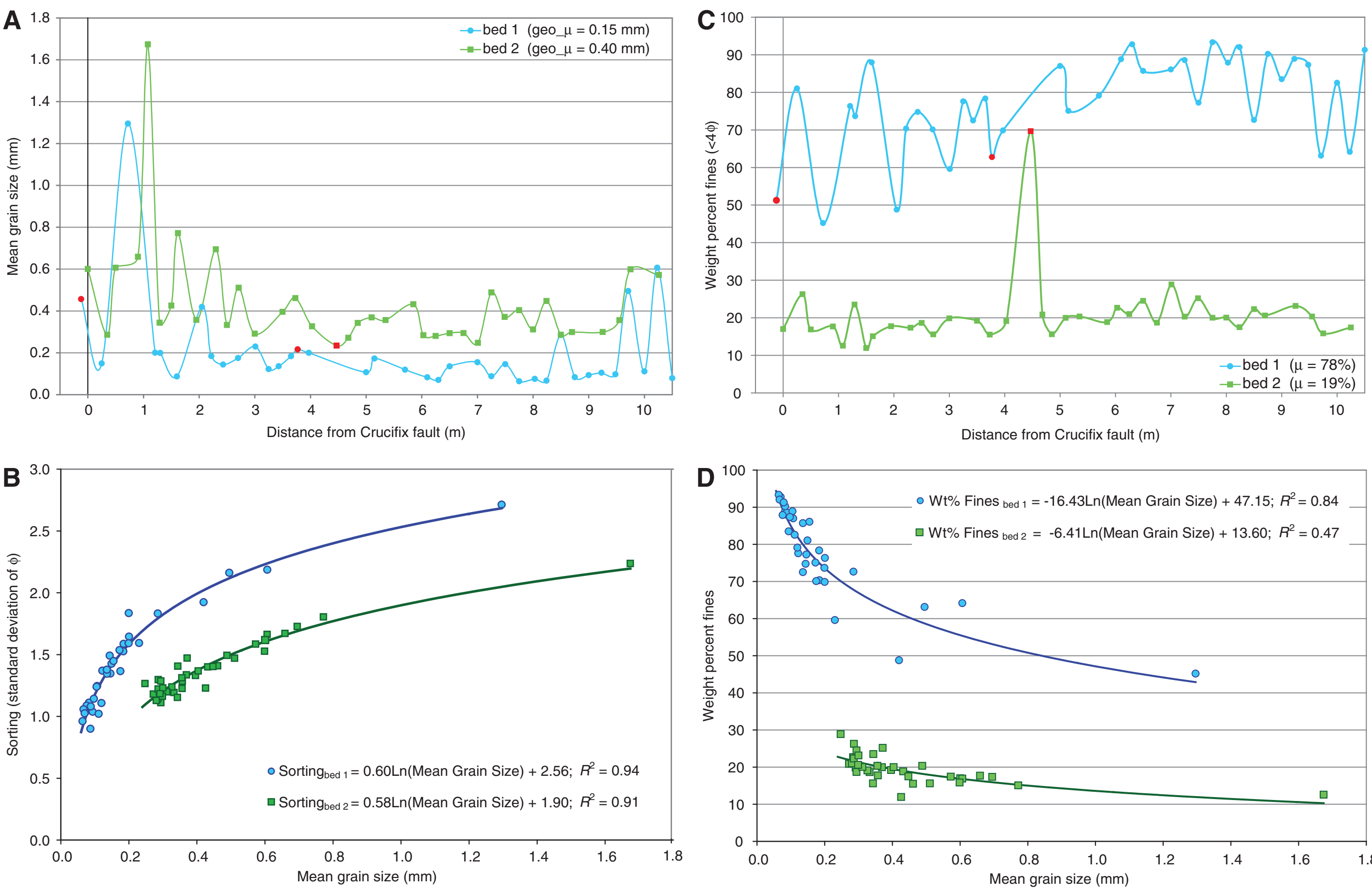


**Figure 7. (A) Primary heterogeneity displayed in terms of average grain size for samples collected from the outcrop surface at permeability test holes in beds 1 and 2. Red points, however, represent the average grain size of fault material located in the associated beds—these data were not used to derive the geometric mean grain size for each bed. (B) Sorting information, given as the standard deviation of grain size measure ϕ for each sample, indicates that bed 1 is more poorly sorted than bed 2, and sorting is predictable as a function of grain size. (C) Weight percent fines of samples from beds 1 and 2. Arithmetic mean is not based on fault samples. (D) Weight percent fines (<4ϕ) as a function of mean grain size.**

cementation related to fluid flow of mineralized water. Average standard deviation values for both beds indicate the deposits are poorly sorted, with bed 1 being more poorly sorted than bed 2 (Fig. 7B), as is expected when comparing an immature primary deposit with a reworked (homogenized) deposit.

A measure of the weight percent fines was calculated for each sample as a proxy for ash content, comminution processes, and/or clay alteration (Fig. 7C). As expected, weight percent fines decrease with increasing mean grain size (Fig. 7D). The fines or ash contents of beds 1 and 2 (Table 1) are consistent with their interpreted lithology and maturity. The weight percent fines within the fault rocks (Table 1, CFa and CFb) represent the percentage of fine-grained material (clay-size fraction) that is, to some extent, a result of cataclasis and associated grain comminution during slip along the fault.

### Petrophysical Observations

Thin-section analyses, XRD techniques, and specific gravity measurements were used to characterize the tuffaceous sediments at the Crucifix site. Glass (shards and pumice fragments), quartz, feldspars, and sanidine are the primary constituents of all outcrop samples (Table 1), with minor amounts of lithic fragments (predominately pumice) and alteration products. Amorphous silica and iron oxides are the primary fillings and coatings along fracture surfaces, with calcite coatings observed locally along the main Crucifix fault and subsidiary faults. The modal content of thin sections, based on petrologic point-count observations, is given in Table 2. Because many units at the Crucifix site are reworked, and our efforts focus on the hydrologic properties of these materials, the mineralogic or textural subdivision of this geologic material (Table 2) was modified from the standard classification schemes for pyroclastic deposits and fragments (% crystals, % glass, % lithics) as Schmid (1981) recommended. The average composition of samples from bed 1 (e.g., Fig. 8A) is 22% crystals, 13% glass or pumice, <1% lithics, <5% iron oxides and

TABLE 2. COMPOSITION OF CRUCIFIX SITE SAMPLES FROM POINT-COUNT THIN-SECTION ANALYSIS

| Sample ID* | Unit/feature sampled | Crystals/crystal fragments | Wt% glass or pumice | Wt% lithics | Wt% matrix (clay/ash mix) | Wt% misc.† |
|---|---|---|---|---|---|---|
| BT-68c | Fault gouge – above survey | 25 | 16 | 3 | 51 | 5 |
| BT-69 | White ash bed *similar to* bed 1 | 9 | 7 | 0 | 82 | 3 |
| BT-90 | Slip surface | 21 | 33 | 3 | 42 | 1 |
| BT-91 | Slip surface | 20 | 19 | <1 | 61 | 0 |
| BT-92 | Bed 2 host rock | 32 | 20 | 10 | 37 | 1 |
| BT-93 | Bed 1 host rock | 15 | 5 | 2 | 71 | 7 |
| BT-104a | Fault gouge | 1 | 21 | 0 | 77 | 0 |
| BT-105 | Fault gouge | 0 | 3 | 0 | 95 | 3 |
| BT-106 | Fault gouge | 41 | 29 | 0 | 27 | 3 |
| BT-107a | Fault gouge | 5 | 8 | 0 | 85 | 1 |
| BT-107b | Fault gouge | <1 | 3 | 0 | 95 | 1 |
| BT-107c | Fault gouge | 23 | 22 | 1 | 51 | 3 |

*Refer to Figure 3 for sample collection location.
†For example, iron oxide, calcite, zeolite, and mica.

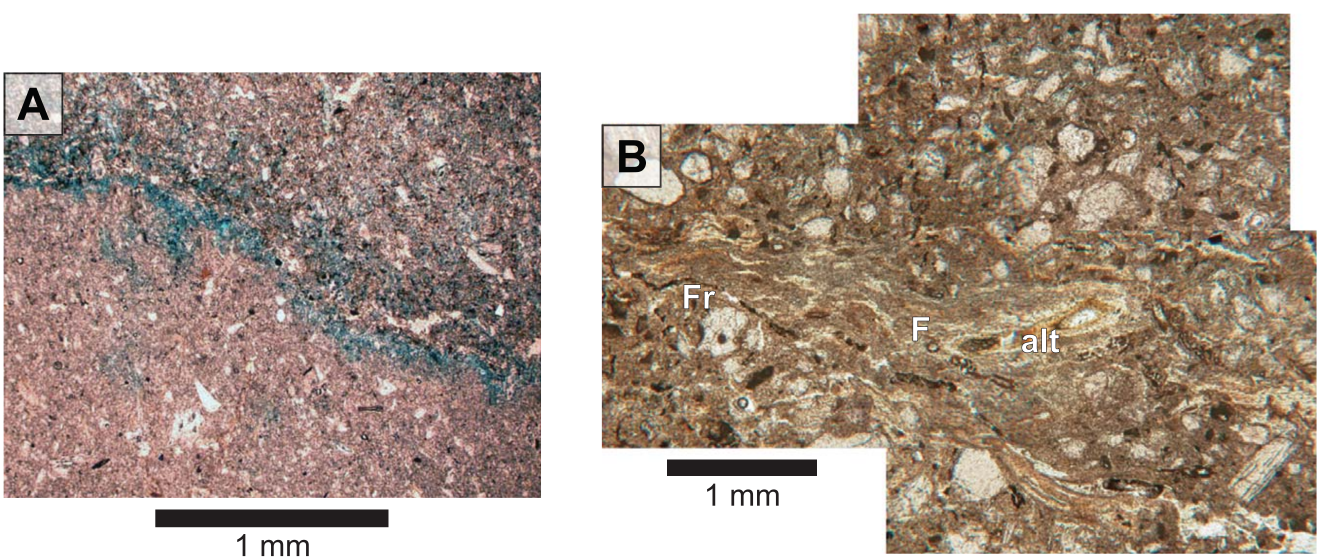


**Figure 8. Compositions and textures of beds 1 and 2. (A) Bed 1 (sample BT-93; see Fig. 3 for location): Dark-colored material near a fracture surface likely results from iron oxide or clay alteration. Blue epoxy infiltrates the matrix from the wall of a hairline fracture surface. (B) Bed 2 (sample BT-62): Dark-brown coating around grains indicates alteration and formation of clay rims. Alteration of glass (alt) within a flattened pumice clast or fiamma (F) also suggests the initial stages of clay formation. Microfracturing (Fr) seen near the fiamma boundary is commonly observed in this material. Microfracture is partially filled with dark-brown clay and iron oxides alternating with silica.**

Lithosphere, published online on 9 January 2012 as doi:10.1130/L179.1


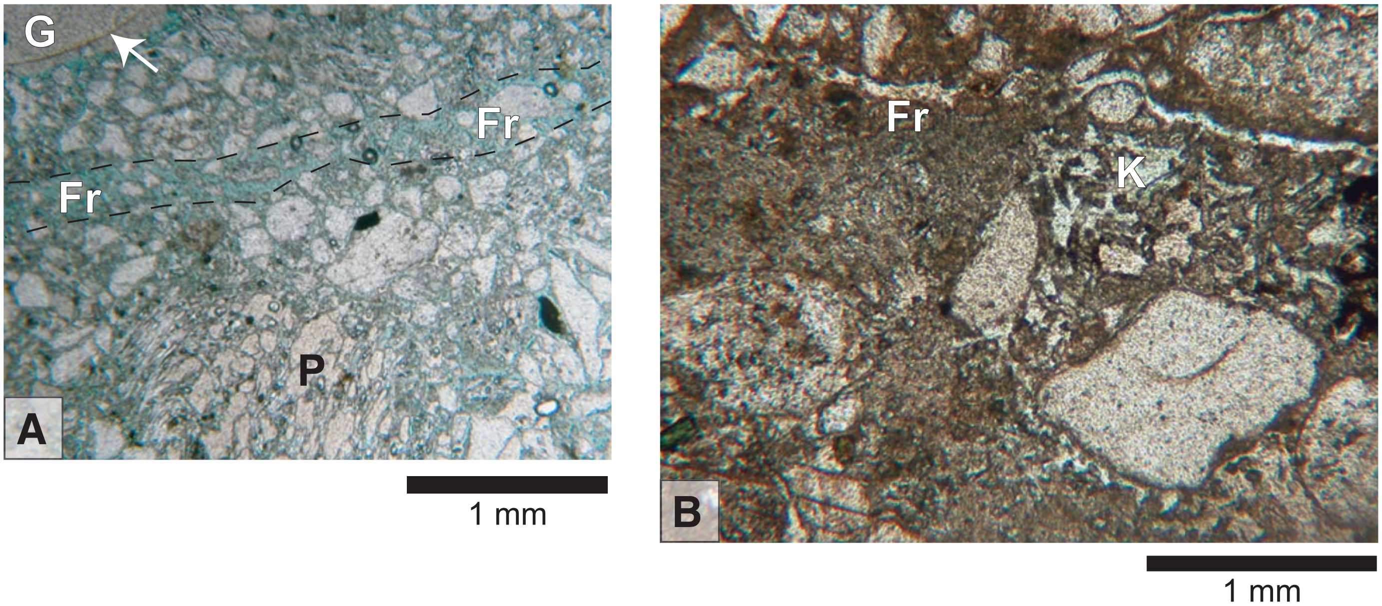


**Figure 9. Photomicrographs of fault located at ~9.65 m (Fig. 3). (A) Sample BT-90 exhibits an amorphous silicic glassy fragment (G) with overgrowth textures, shown by an arrow pointing to the original grain boundary. P—pumice clast; Fr—fracture and dilation band. (B) Sample BT-91 collected from contact of 1-cm-thick fault surface with bed 2. Crystal fragments and glass shards are supported by a fine-grained matrix of glass and clay. A zone of fine-grained clay surrounds the outer walls of open hairline microfracture surfaces (Fr), illustrating a mixed zone of deformation, including cataclasis and dilation. The wormlike texture labeled K is vermicular kaolinite. The well-developed vermicular texture suggests the clay is authigenic pore-filling cement that formed in situ, likely a result of diagenesis.**

alteration products, and 60% fine-grained matrix (ash and glass), whereas the average composition of samples from bed 2 (e.g., Fig. 8B) is 32% crystals, 20% glass or pumice, 10% lithics, and 37% fine-grained matrix (Table 1). These results are consistent with the weight percent fines determined for each bed through grain-size analysis (Fig. 7C). Crucifix fault core samples consist of, on average, 11% crystals, 14% glass or pumice, 2% lithics, 70% fine-grained material, and 3% miscellaneous constituents, such as calcite (Table 1). Slip surface samples from a 0.095-m-displacement fault located ~9.65 m along the transect (see Fig. 3) consist of 20% crystals, 26% glass or pumice, 2% lithics, and 51% fine-grained matrix (Table 1).

Identification of minerals within the fine-grained material by point counting was difficult because of the fuzzy texture imparted by the abundance of altered glass shards in the samples. XRD techniques were used to identify clays or other alteration products within the matrix material and fine-grained fault gouge. Quartz, amorphous silica, glass, feldspars, tridymite, cristobolite, and mica are the primary constituents of these sediments. The presence of quartz–tridymite–cristobolite–feldspar assemblages suggests some devitrification and alteration of glassy constituents in the sampled beds and more so within the fault zones (Vaniman et al., 2001; Evans and Bradbury, 2004). Minor to trace amounts of aluminosilicates, iron oxides, calcite, and amorphous aluminum hydroxides were also observed. Clay minerals identified in several samples include kaolinite and illite. Trace amounts of hydrated aluminosilicates and zeolites (analcime, clinoptilolite, laumontite) were found in a few samples and are likely the result of the initial stages of glass alteration.

Photomicrographs of textural and structural deformation elements (Figs. 8–12) further convey their characteristics and potential influence on permeability architecture. Blue-dyed epoxy was injected into the samples to impregnate pores and show microporosity in thin sections. Material from bed 1, collected ~5.2 m east of the Crucifix fault (as shown in Fig. 3), consists of delicate glass shards and quartz within a fine-grained glass- and clay-rich matrix (Fig. 8A). Trace amounts of kaolinite and iron-oxide alteration are evident from XRD analysis. A felty to fuzzy texture is observed with magnification, which may indicate partial devitrification. Injection of blue epoxy into this sample shows microfractures, which have the potential to control flow within this thin and porous ash layer. The blue epoxy did not impregnate (fully fill) the microfracture but rather focused around the outer edges of the fracture, impregnating the surrounding matrix. Material from bed 2, collected ~9 m east of the Crucifix fault (as shown in Fig. 3), shows a fiamma, or flame-

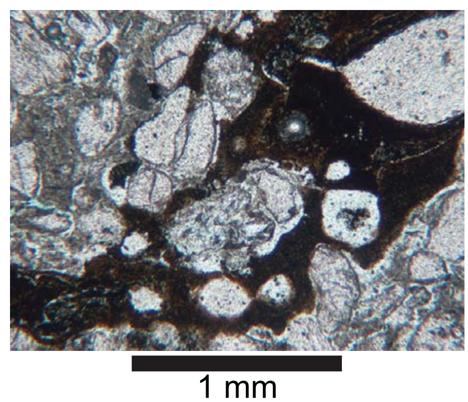


**Figure 10. Quartz overgrowth textures, clay alteration of material adjacent to fracture wall, and dark brown iron-oxide fracture in-fillings support interpretation of multiple phases of fluid rock interactions. Sample BT-106 was collected near the eastern conjugate fault at ~4.7 m (Fig. 3). A large curvilinear fracture illustrates entrainment of grains from wall boundaries and is filled with iron oxides, clay, and glass altering to zeolite. Note presence of blue epoxy in oblique extensional microfractures.**

shaped structure, the relict of a devitrified collapsed pumice clast (Fig. 8B). Alteration of glass within this clast and the brownish hue of the matrix also suggest clay transformation processes. The dark-brown coating around several

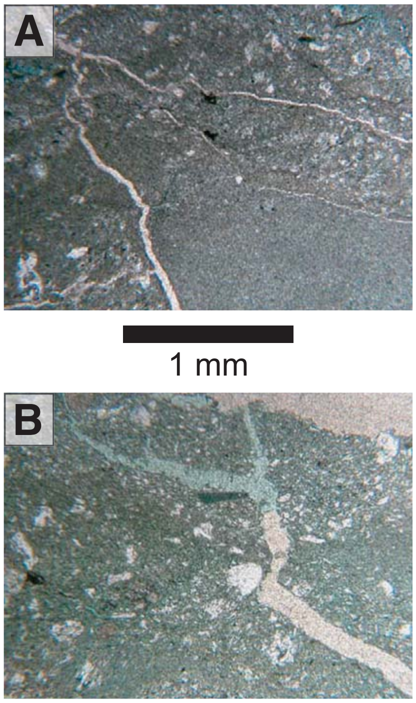


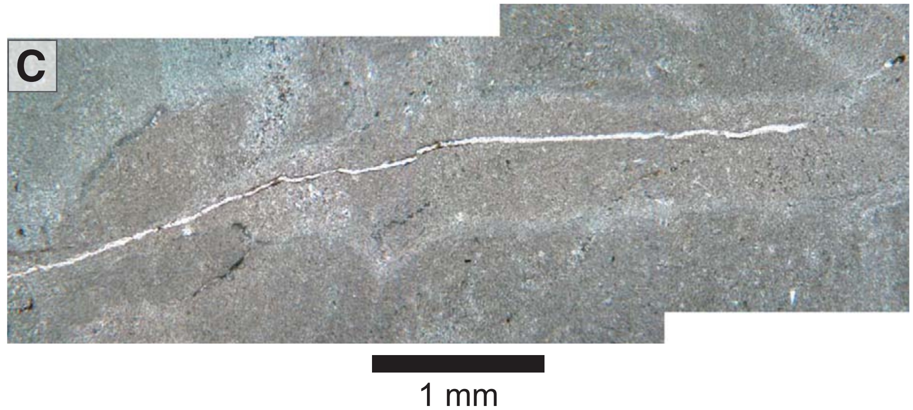


**Figure 11. Crucifix fault core. (A) Sample BT-104a was collected from the easternmost layer inside the Crucifix fault core (Fig. 3). Abrasion, mixing, and dragging of adjacent beds, as observed at the outcrop scale, result in abundant crystal and glass fragments observed at the micrometer scale. (B) Disaggregation of coarse to fine grains (sample BT-104) suggests granular flow and grain-boundary sliding processes within the outer fault core (cf. Rawling and Goodwin, 2003; Fossen et al., 2007). Blue epoxy pattern illustrates partial fracture filling. (C) Sample BT-105 was collected perpendicular to fault strike on western edge of the Crucifix fault. A halo of light-colored, convoluted clay and glassy ash surround an intracore microfracture, which is then surrounded by another halo of micrometer-thick bleached material. The microfracture does not absorb the blue epoxy, unlike the surrounding clay layer.**

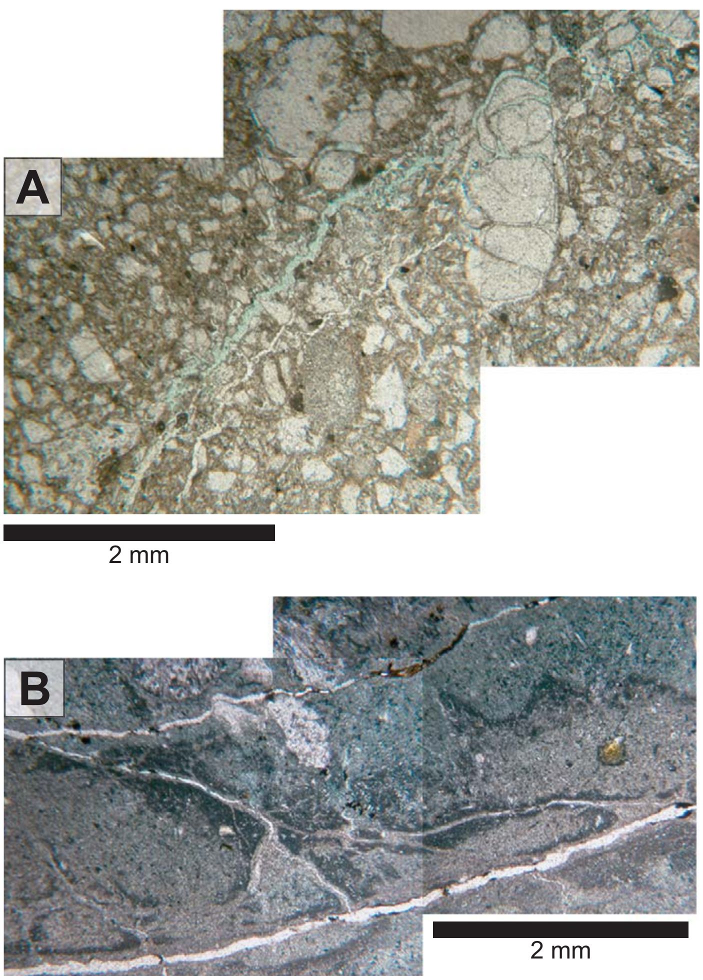


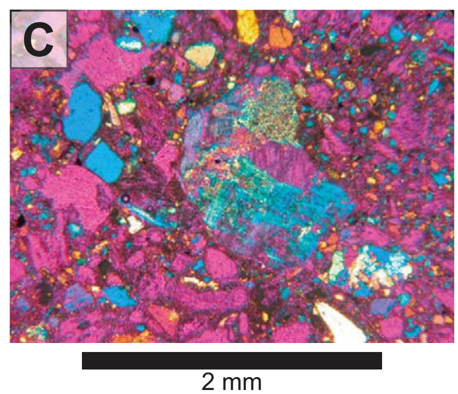


**Figure 12. Crucifix fault deformation microstructures illustrate layered heterogeneity with varying textural and lithological characteristics. (A) Sample BT-107a, from a western section of gouge (Figs. 3 and 4B), shows perlitic fracturing in a glassy fragment. Open microfractures absorb blue epoxy, while filled fractures do not. A brownish matrix of clay, volcanic ash, and glass is observed, and crystal fragments are abundant. (B) Sample BT-107b, from the central fault core gouge zone (Fig. 4B), illustrates a layered and locally convoluted, fine-grained clay and ash having multiple fractures filled with silica and bounded by layers of clay—shown in alternating light and dark colors. Iron-oxide–rich clays are shown in the upper microfracture and in an altered glassy fragment. Blue epoxy in the upper half of the photomicrograph does not extend below the fracture oblique to the sections. (C) Sample BT-107c (Fig. 4B), shown in cross-polarized light with the gypsum plate inserted. A deformed feldspar clast with sericitic alteration is surrounded by a zone of fine-grained cataclasis that is characterized by rotated grains and microfractures, pumice and glass fragments, quartz clast, and fine-grained clay.**

Lithosphere, published online on 9 January 2012 as doi:10.1130/L179.1


individual grains indicates the alteration of glass and formation of clay rims. Material composition is volcanic glass, quartz, feldspars, ash, and clay. Bed 2 is coarser than bed 1 and contains less ash.

Photomicrographs of fault samples collected in the Crucifix fault footwall block at ~9.65 m (as shown in Fig. 3) illustrate features and deformation mechanisms (Fig. 9) associated with a complex history of deformation—a cyclic history that should yield heterogeneous permeability architecture. For example, the development of overgrowth textures, thought to occur through diffusive mass transfer, is observed (Fig. 9A). Overgrowth textures can locally reduce porosity. In the same thin section, however, dilation mechanisms are observed, with blue epoxy filling pore spaces of both the matrix and a fracture. The presence of the clay mineral kaolinite (Fig. 9B) suggests hydration and alteration of glass. Hydration is an important process because it may locally reduce porosity and permeability.

The intensity of microscale deformation features increases in samples collected nearer to the Crucifix fault. A sample from a fault surface near the eastern conjugate fault (~4.9 m along the transect; Fig. 3) and in an intensely fractured region of the footwall damage zone shows iron oxide and clay in-filling a fracture within the fault zone (Fig. 10). Kaolinite and the zeolite analcime were detected with XRD. Open microfractures oblique to the clay-filled fracture are evident by the presence of blue-dyed epoxy. Rounding of grains and development of clay rims surrounding the grains coupled with fine-grained comminuted material are observed as a result of cataclastic deformation and alteration associated with fluid rock interactions.

Several core samples from the main Crucifix fault illustrate compositional and textural variations both parallel and perpendicular to the fault trace (Figs. 11 and 12). Bounding slip surfaces transition to vertical layers of ash and sand, to mixed grain sizes, to a core that is composed of very-fine–grained comminuted material intermixed with lithic fragments and convoluted clay gouge (Fig. 12B). Disaggregated grains are observed surrounding a finer phyllosilicate band in the easternmost layer in the fault core (Fig. 11). The central core exhibits the finest grain clay gouge and comminuted ash with micrometer-scale fractures (Fig. 12B). Abundant crystal and glass fragments are found near the edge of the fault core (Fig. 11A). Mineralized and open fractures are found throughout the edges of the core, and some fractures exhibit both characteristics (Figs. 11B and 12A). Partial mineralization may affect the overall porosity and permeability of fracture systems. Fractures also commonly splay into several microfractures near their tips (Fig. 11B).

XRD analysis suggests the presence of illite, kaolinite, amorphous silica (glass), quartz, sanidine, and trace zeolites. Irregular geometry, distribution, and discoloration of the clay core and surrounding comminuted material (Fig. 11C) are possible evidence that (1) the fault core was subject to at least minor fluid intrusion contemporaneous with shear strain or (2) grain comminution led to capillary storage of fluids along the slip surface. Lighter clay gouge immediately surrounding an open to partially mineralized fracture surface is further surrounded by a bleached rim and darker gouge. These features suggest a complex fault-zone evolution that involved multiple episodes of fluid rock interactions. Overall, the lithological and petrophysical properties of the fault core vary both across- and along-fault at the micrometer scale.

**Porosity and Gas Permeability**

The sampled beds are highly porous, with bed 1 locally more porous than bed 2; conversely, samples from the Crucifix fault and subsidiary faults yield a wider spectrum of values (Table 1). Samples from poorly sorted and fines-enriched bed 1 were more porous than samples from the reworked, more mature bed 2, which is a nonintuitive result that may reflect the limited number of samples examined, or perhaps that disconnected pumiceous porosity in bed 1 is a significant fraction of the total porosity value. For comparison, nonweathered volcanic tuff and ash typically have porosity ranging from 14% to 50% (weathering can increase this to greater than 60%; Fetter, 1994), and unconsolidated deposits of silt and clay exhibit porosities ranging from 35% to 50% (Davis, 1969).

Permeability data from both beds are highly skewed toward lower values (Fig. 13); therefore, the geometric mean is the appropriate measure of central tendency for this parameter. On average, the primary or slack-water–deposited ash-fall material of bed 1 exhibits a larger permeability value (342 mD) than the more homogeneous reworked pumiceous tephra of bed 2 (254 mD). The two populations exhibit essentially the same level of variability (arithmetic coefficient of variation for each bed is 1.20), and they both exhibit the presence of erratically large values (arithmetic coefficient of variation >1) at similar distances from the Crucifix fault (Fig. 13), suggesting that secondary heterogeneities in both beds are attributable to some combination of diagenetic and deformation processes between 0 and 10.5 m along the transects. Between 10.5 and 16.5 m, large permeability values (especially near 14 m along transect; Fig. 13) probably reflect the intersection of test holes with vertical fractures connected to the exposure surface. If an important heterogeneity, such as an open fracture, spatially coincides with a heavily weighted portion of the flow system, its presence is manifested in the measured value. If an important heterogeneity does not coincide with the region of heavy weighting, its presence may go unnoticed (cf. Molz et al., 2003).

Bed 1 is more poorly sorted (more heterogeneous) and has a smaller average grain size and greater weight percent fines compared to bed 2, yet bed 1 is also more porous and slightly more permeable. The higher average permeability value may be attributed to sintering of grains, observed in thin sections, in the bed 1 ash-fall deposit. Sintering can lead to more brittle deformation and the development of more intense fracturing and microfracturing. This interpretation is supported by higher fracture densities in bed 1 compared to bed 2 (Fig. 5). The average permeability of the two lithologic beds, however, is not significantly different.

The limited number of samples collected for laboratory analysis of specific gravity precludes, at this time, correlation of our permeability data with porosity—a technique others have shown (Istok et al., 1994; Rautman et al., 1995; Flint and Selker, 2003) to be particularly effective for estimating $k$ in terms of porosity over the vertical thickness of a tuff sequence, given clear deterministic relationships in the vertical direction that result from compositional and textural differences as well as postdepositional alteration. Our motivation, however, is to understand the stochastic and secondarily induced lateral heterogeneity of hydrologic properties within individual nonwelded units, given the potential effect on the length scale of lateral flow in such units. There is probably little value in using porosity as a predictor for permeability in the lateral, fractured, intra-unit case. For example, the presence of microfractures has been shown to reduce any such correlation (cf. Flint and Selker, 2003).

In comparison to permeability measured by Dinwiddie et al. (2006) for faulted nonwelded to sintered ignimbrite of the Bishop Tuff (Chalk Cove site), the permeability distribution for sediments at the Crucifix site is more heterogeneous. The host-rock permeability for nonwelded ignimbrites of the Bishop Tuff averaged 120 mD, with a standard deviation of 5 mD (Dinwiddie et al., 2006). Fault-zone deformation generally increased the heterogeneity of the pyroclastic deposits at the Chalk Cove site by less than a factor of five, with all measurements being restricted to less than two orders of magnitude variation (Dinwiddie et al., 2006). Note that the permeabilities of large-scale (i.e., ~20-m-long) open fractures at

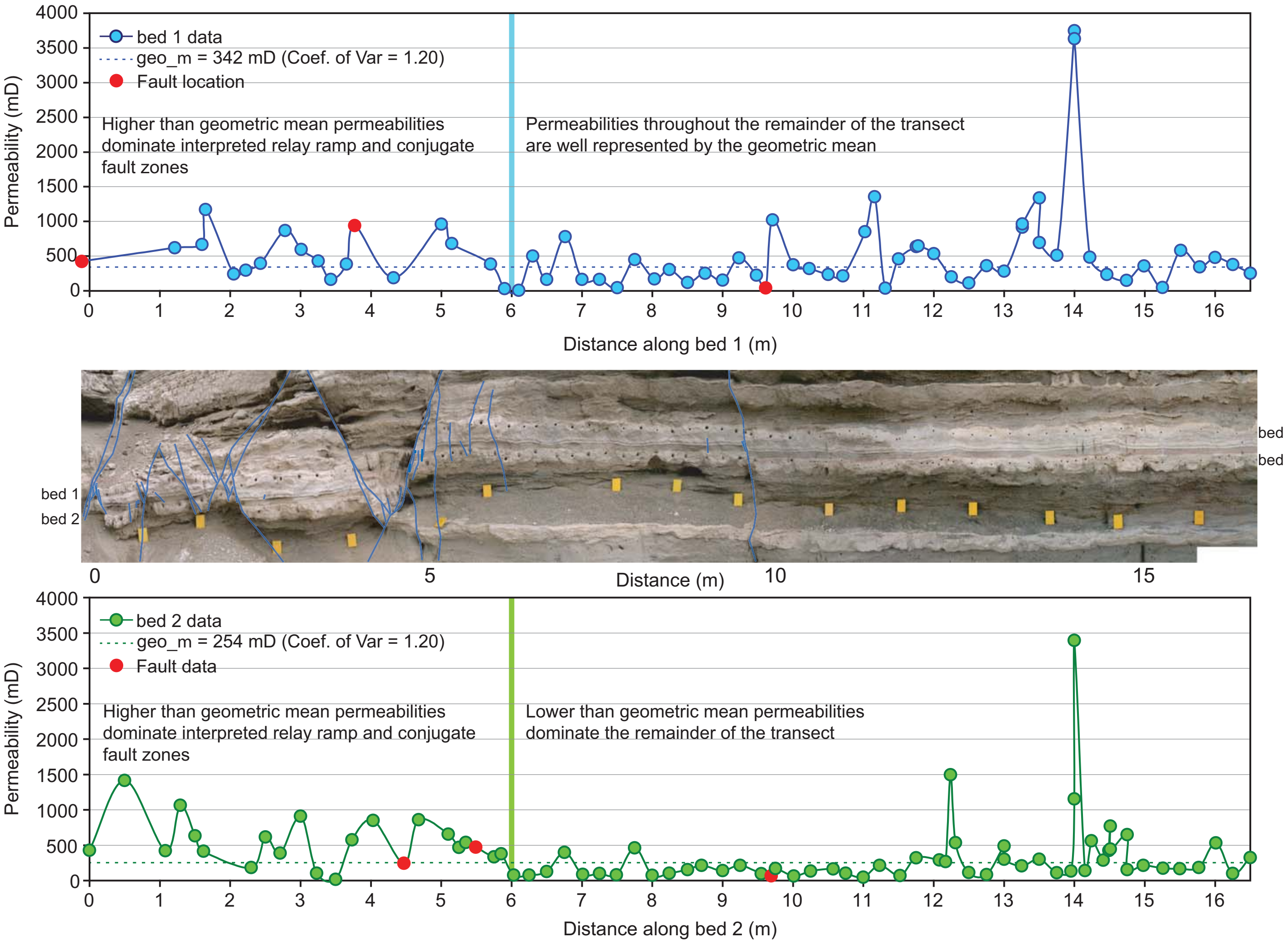


**Figure 13. Permeability heterogeneity in the footwall of the Crucifix fault. Red points represent data from test holes intersecting fault material located in the associated beds—these data are hybrid combinations of permeability from fault material and permeability of adjacent nonfaulted bed material and were not used to derive the geometric mean permeability for each bed. Higher than average values dominate the interpreted relay ramp and conjugate fault zone within each bed.**

the Chalk Cove site were not measured by the minipermeametry method.

At the Crucifix site, however, the lithology of the host sediment and the potential for multiple episodes of deformation combine to create permeability heterogeneities spanning more than three orders of magnitude; both smaller and larger values of permeability were measured at the Crucifix site relative to the Chalk Cove site. Permeability ranges from 6 mD to nearly 4 D in bed 1, and from 15 mD to more than 3 D in bed 2 (Fig. 13). Fewer permeability measurements were collected in the vicinity of the Crucifix fault and its footwall damage zone due to the friable and highly weathered nature of the deformed beds in this area. Although sparse, higher than average permeability values were generally measured near the Crucifix fault (i.e., between 0 and 6 m; Fig. 13). Beyond this footwall zone, there are approximately as many permeability values higher than the average as there are values lower than the average within bed 1, but values lower than the average dominate within bed 2. Intense deformation in the damage zone weakened the sediments and almost certainly led to higher matrix permeability values in highly fractured areas adjacent to slip surfaces and potentially to low permeability values trending perpendicular to the fault core where clay or clay transformation processes are present. Sparse data collected within various layers of the Crucifix fault core (see Fig. 4B) ranged between 114 and 933 mD, varying by less than one order of magnitude.

For these faulted and fractured granular porous media, we do not develop a formula that relates permeability ($k$) to grain-size ($d$) data, because poor sorting exhibited by the sampled units and their enhanced permeability associated with fracturing prohibit using phenomenological $k = Cd^2$ formulations. We do not develop a formula that relates permeability to fracture aperture because our measured permeability is neither strictly matrix permeability nor strictly fracture permeability; rather, it is matrix permeability variably influenced by the presence of local fractures.

Areal fracture density data are generally not well correlated with permeability data, perhaps because the fracture survey included all features within a 25-cm-diameter area centered around each test hole, including bounding beds to distances of several centimeters above and below beds 1 and 2, whereas permeability data were

Lithosphere, published online on 9 January 2012 as doi:10.1130/L179.1


measured within beds 1 and 2 at the distal ends of 10-cm-deep test holes by an instrument with a very localized averaging volume and highly nonlinear weighting (Molz et al., 2003; Dinwiddie, 2005). One exception is observed in the positive correlation between permeability and areal fracture density data from bed 2 at locations influenced only by conjugate (and not vertical) fracturing, wherein 60% of the observed variation is explained by a linear regression (Fig. 14). After eliminating the one datum in this series that was directly influenced by the presence of a fault, 80% of the observed variation is explained by a linear regression. It is also informative to observe zones of relatively high and low areal conjugate fracture density and permeability throughout the sampled exposure (Figs. 5 and 13). Had a <25-cm-diameter area been used to measure the occurrence of fractures, measured areal fracture densities would likely have decreased, perhaps decreasing more in some locations than others. The degree to which correlation between areal fracture density and permeability may have improved, however, is unclear and out of the scope of this analysis.

## DISCUSSION

### Lithologic and Structural Controls that Influence Permeability

Several features of the Crucifix site illustrate the lithologic heterogeneity, exposure-scale symmetric to meter-scale asymmetric structural geometry, and hydrogeologic heterogeneity of poorly to nonlithified sequences. The Crucifix fault core composition varies both vertically and horizontally along the length and width of the slip surfaces. Hanging-wall deformation occurs west of the fault trace at the scan line and extends only centimeters to decimeters, whereas footwall deformation extends ~10 m east of the fault trace. In addition, the footwall damage zone width (defined here as the width over which conjugate areal fracture density is greater than zero) varies little between the two lithologically distinct beds (Fig. 5): for both beds 1 and 2, conjugate deformation features (faults and fractures) are present to ~6 m into the footwall with slight variations, excluding a very narrow damage zone in each bed associated with the small-displacement fault located at 9.65 m along the scan-line transect. We interpret the zone between the Crucifix fault and the parallel conjugate fault as a section through a relay ramp. Relay ramps are usually zones of localized high strain and high permeability (Ferrill and Morris, 2001). This zone at the Crucifix site coincides with maximum deformation by all the measures employed—bed tilt, fault density, areal conjugate fracture density, generally higher than average gas permeabilities, and higher than average subsurface resistivities.

Deformation style in an individual bed (Figs. 4 and 5) is related to a number of properties that include structural position, grain size, weight percent fines, ash content, and bed thickness. Bed 1 is entrained farther downdip into the Crucifix fault zone than bed 2, probably because bed 1 has more ash and fines, is thinner, and has a greater potential for clay transformation and smear, which may facilitate its ductile incorporation into the fault zone—especially with the influx of fluids during faulting. In less-deformed areas of the fault core, bed 1 demonstrates a brittle style of deformation with numerous short trace-length fractures that appear coated or mineralized in thin section (Fig. 11A). Bed 1 may indeed be a primary ash-fall deposit rather than a slack-water deposit, because we observe the effects of sintering at the microscopic scale. Such features would likely alter relatively quickly in the presence of fluids. Fine-grained material exhibits interlocking grain boundaries and has a fuzzy and indistinct quality when magnified. In a nondeformed unit, sintering will reduce porosity; however, in a deformed unit, brittle failure along sintered grain boundaries may result in increased microfracturing, which may increase its secondary porosity and permeability. Immediately adjacent to the Crucifix fault core, the coarser and relatively ash-poor bed 2 typically comprises the outer bounding layer and heavily mixed zones of the fault core. At increasing distances from the fault, bed 2 is characterized by open dilatant fractures that are mineralized with clay or iron oxides (Figs. 11B and 12).

Capillary theory suggests that open subvertical fractures will hinder lateral flow under less than fully saturated conditions because capillary attraction is greater within the matrix than within open fractures. Filled subvertical fractures will function either as capillary or permeability barriers to constrain lateral flow, depending on the hydrologic properties of the fracture filling relative to those of the adjacent matrix.

The distribution and textural characteristics of structural deformation features may locally influence porosity and permeability variations within beds 1 and 2. For example, thin sections show that dilation and disaggregation bands (Du Bernard et al., 2002; Fossen et al., 2007) occur primarily within bed 2 (the reworked tephra-fall deposit). Dilation bands may locally increase porosity (observe blue epoxy highlighting a fracture surface in Fig. 12A) and permeability (Fig. 14); however, these properties may also be controlled by local variations in grain size and structural position relative to the main or subsidiary faults (Fig. 7). Dilation bands also occur in the white ash of bed 1; however, they are very narrow, and depending on the position and amount of clay transformation, they may locally and slightly increase or decrease permeability (Figs. 8A and 13). In the Crucifix fault core, porosity and permeability vary (Table 1,

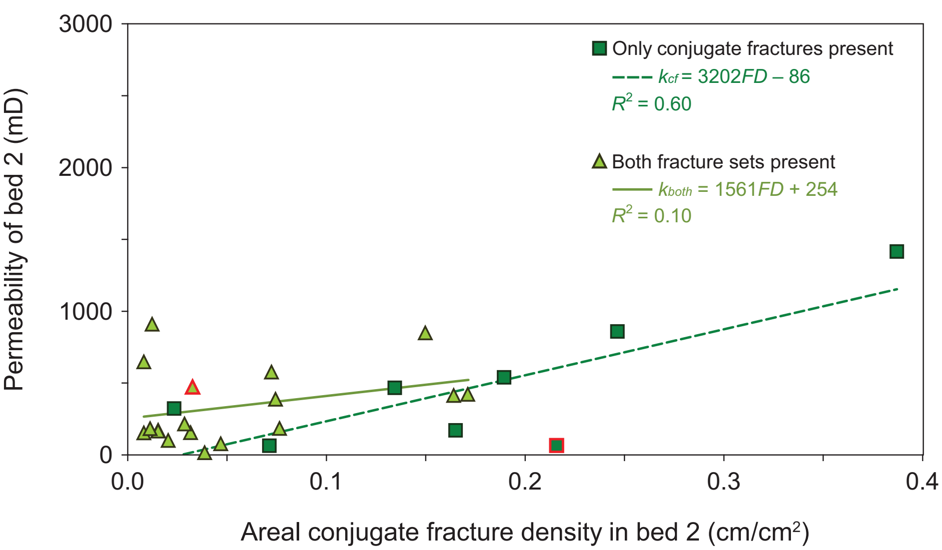


**Figure 14. Cross plot of permeability and areal conjugate fracture density for bed 2 indicates positive correlation. Permeability data are shown once in one of two series, namely, where associated with only conjugate fractures, $k_{cf}$, and where associated with the occurrence of both vertical and conjugate fracture sets, $k_{both}$. Data outlined in red represent test holes intersecting fault material and thus a hybrid combination of permeability from fault material and adjacent nonfaulted bed material. FD—areal conjugate fracture density.**

CFa; Fig. 4B) with grain-size and clay alteration (Figs. 11 and 12) as a result of multiple layers of intensely deformed, very fine-grained material occurring adjacent to lenses of less-deformed, poorly sorted material (Fig. 12). Thin sections from the Crucifix fault core (Fig. 12) illustrate zones of cataclastic deformation and porosity reduction that surround a damage zone of dilatant microfracturing, similar to the results of Main et al. (2001).

Our results are consistent with several other studies (e.g., Cashman and Cashman, 2000; Du Bernard et al., 2002; Rawling and Goodwin, 2003; Cashman et al., 2007), which have shown that in addition to brittle deformation mechanisms (such as cataclasis, dilation, and transgranular fracturing), poorly lithified siliciclastic sediments also exhibit distributed deformation and deformation by ductile micromechanisms. The Crucifix site is unique, however, when compared to recent studies of sandstones and other poorly consolidated deposits (Caine et al., 1996; Du Bernard et al., 2002; Rawling and Goodwin, 2003; Bense and Person, 2006) because its material composition includes abundant glassy fragments and ash. Physical analog modeling by Wolf (2003) has shown that less strain is required to develop shear bands in glass beads than in sand, and that grain size and bed thickness can influence the spacing and overall shape of shear bands. Differences in deformation characteristics observed between beds 1 and 2 may also be influenced by the local presence or absence of glassy fragments or ash.

Two localized zones of high resistivity occur within the subsurface footwall of the Crucifix fault: (1) between the Crucifix fault and the parallel crossing conjugate fault and (2) at the same elevation but between the conjugate fault and the small-displacement fault that is located ~10 m along the geophysics transect (Fig. 6). These data suggest that the zone of subsurface deformation is up to 10 m wide in the Crucifix footwall, similar to observations above road level. When we combine knowledge of site geology (i.e., vertically layered, relatively homogeneous, laterally continuous, horizontal to subhorizontal beds are occasionally disrupted by faults, submeter- to meter-scale fluvial channels, and rare pinch-outs) with these resistivity data, we interpret that these localized zones of high resistivity are locally drier, intrinsic permeability within the damage zones is high (such that they are capable of transmitting water and solutes rapidly downward in the form of film or rivulet flow), and fluid flow is laterally compartmentalized. Resistivity data suggest the damage zone immediately surrounding the eastern horst-bounding fault, except at the very near surface, is less extensive than that of the Crucifix fault, that intrinsic permeability is lower, and that the narrow fault zone is more highly saturated, as are the units it dissects. One could infer that at this elevation that the Crucifix fault acts as a subvertical capillary barrier, while the eastern horst-bounding fault acts as a subvertical permeability barrier.

East of the western horst-bounding (Crucifix) fault, there is a very broad, 60-m-long, near-continuous, but vertically limited, electrically conductive unit at elevations between 1285 and 1284 m. This zone significantly attenuates the radar signal such that few features are observed below this level in radargrams.

West of the eastern horst-bounding fault, there is a very broad zone of moderately high to high resistivities that dominates a region characterized in radar data by significant bedding disruptions, some beds that are tilted by 3.2°, and deep signal penetration. The highest resistivities in this broad zone are laterally congruous with bedding disruptions. Bedding disruptions observed at the Crucifix site exposure are attributed to three principal features: (1) rare pinch-outs of otherwise laterally continuous beds, (2) occasional submeter- to meter-scale fluvial channels, and (3) faults. Knowledge of site geology combined with the relatively high resistivities and the significant improvement in radar signal penetration depth within this broad zone suggest that these deposits are locally drier, that intrinsic permeability is relatively high, and that soil moisture may not be stagnant, especially where local deformation features induce secondary porosity and permeability on the protolith. While not interpreted in Figure 6, bedding disruptions within this zone may represent faults that tip out in the subsurface within a broad footwall deformation zone associated with the eastern horst-bounding fault; however, similar deformation is not observed in the surface exposure above road level.

Structural deformation observed at the Crucifix site is thought to overprint additional heterogeneities onto the primary permeability of the ash-fall (bed 1) and reworked tephra-fall (bed 2) units, thereby influencing permeability architecture (see Figs. 5, 13, and 14). Locally, permeability variations are observed in both beds (Fig. 13) where small-displacement faults and conjugate fractures are clustered between the Crucifix fault and the crossing conjugate faults (Figs. 4 and 5). Cataclastic fault-zone deformation involves grain cracking and crushing, with grain-size and pore-volume reduction that may result in the development of low-permeability fault gouge. Water flowing laterally above a capillary or permeability barrier in a gently sloping unit could be interrupted and focused downward along a steeply dipping fault, if the unit had been locally incorporated into the fault core. At a greater distance away from the main fault traces, open vertical fractures and open conjugate fractures should create more permeable beds together than would be exhibited by nondeformed host rock, although this cannot be objectively demonstrated given the lack of information about the permeability of the beds prior to their deformation. However, permeability increases are observed within bed 2 with increasing areal conjugate fracture density (Fig. 14).

In the variably saturated vadose zone, the influence of localized low- and high-permeability elements on water movement depends on the state of saturation. Under locally saturated conditions, cataclastic fault gouge will behave as a barrier, while open fractures will behave as conduits. Under unsaturated conditions, water may wick into and be retained in fine-grained fault gouge, open fractures may behave as capillary barriers that cause water to be retained within the smaller pores of adjacent host rock, and filled fractures may behave as permeability barriers that prevent cross-block flow (Fedors et al., 2002). The temporal and spatial evolution of a fault will influence the distribution and nature of fractures and the overall structural and permeability architecture of the fault zone. Microfractures may intermittently be open following their initial formation and prior to fluid infiltration, which may result in full to partial healing of fractures due to precipitation of carbonates, iron oxides, or clays. Subsequent deformation events may reopen or partially reopen fractures or reactivate zones of weakness that result from variations in composition and frictional properties.

Hydraulic anisotropy in siliciclastic fault zones at the millimeter to centimeter scale is expected to result from clay smearing, grain reorientation, bed drag, and vertical segmentation of the fault plane (mechanisms described by Bense and Person, 2006)—we observed the end result of these mechanisms on fault fabric and electrical resistivity at the Crucifix site. The Crucifix fault core and the associated crossing conjugate normal faults in the footwall deformation zone should create permeability anisotropy at the centimeter to meter scale (Ferrill et al., 2000, 2009; Evans and Bradbury, 2004). This type of fault system is expected to influence fluid flow both laterally and vertically. Bed-parallel lateral fluid movement should be restricted horizontally by faults behaving as flow barriers, whereas along-fault vertical fluid movement should be focused downdip. Where conjugate faults are present, influences such as these may combine to enhance localized fluid flow in a direction parallel to the intersection line of the faults (McGinnis et al., 2009).

Microscopic analyses indicate clay forms (1) as a function of diagenesis related to the alteration of glass and feldspars (Fig. 9A) and (2) as a result of ductile deformation along the faults (Figs. 11C and 12B). The presence and distribution of clays within these beds and faults are important because recent work suggests that neomineralized clay growth or alteration may play a significant role in the mechanical behavior of a fault (Schleicher et al., 2006, 2010). The development of clays and discontinuous iron-oxide fillings, the weathering of feldspars to fine-grained clays, and discoloration surrounding fractures are observed in several samples from the Crucifix site (e.g., Fig. 12B) and suggest the presence of fluids and alteration processes during deformation. The glass content of ash-rich layers or lenses may contribute to the brittle deformation style observed at the Crucifix site. The abundant volcanic ash within the primary or slack-water–deposited ash-fall and the reworked tephra-fall deposits may have behaved as a lubricant when hydrated (similar to the behavior of fly ash as a concrete additive that initially assists with fluidization and ultimately enhances strength; Muhunthan et al., 2004; Copeland, 2003), leading to fluidization of ash-rich material within and bed drag into these fault zones. As water left the system, the volcanic ash may have chemically reacted with calcium and oxides to produce a less permeable and a relatively more cohesive material. In summary, the ash content of individual bedded tuff units will likely affect the nature of small-scale deformation features associated with subvertical faults that cut through the bedded units.

### Implications for Fluid Flow

Hydrologic numerical models are often constructed using assumptions that stratigraphic contacts have smooth boundaries and exhibit sharp hydrologic property contrasts. Both of these assumptions promote lateral flow in numerical models (Flint et al., 2003). The photomosaic of bedded units at the Crucifix site (Fig. 3) illustrates the undulatory nature of the stratigraphic surfaces, which are nonmonotonically continuous for 78.5 m, except where interrupted by fault offsets, small fluvial channels, and occasional pinch-outs. The geometric mean permeabilities calculated for the two lithologically distinct, bedded units sampled at the Crucifix site do not exhibit sharp contrasts; rather, the hydrologic property variations (attributed to structural deformation) within the individual beds are more remarkable (Fig. 13). Steeply dipping or vertical fractures, whether open (a subvertical capillary barrier) or filled (a subvertical permeability barrier), will locally compartmentalize and promote vertical flow and thereby constrain lateral flow (Fedors et al., 2002).

## CONCLUSIONS

Analyses of tuffaceous sediments at the Crucifix site underscore three classes of fault-zone deformation features, originally observed by the authors in massive nonwelded ignimbrite units of the Bishop Tuff (Dinwiddie et al., 2006), that may constrain lateral flow in unsaturated bedded tuffs: (1) cataclasis resulting in fine-grained fault gouge, (2) mappable open fractures, and (3) microfractures, microfaults, and grain rotation, resulting in additional connected porosity in matrix blocks adjacent the fault. The following additional features of lithology-dependent fault-zone deformation, which further our understanding of expected flow behavior for bedded tuffs, were recognized at the Crucifix site:

(1) Clay smear, bed drag, and vertical segmentation create permeability anisotropy along the Crucifix fault core.
(2) Distributed damage in a probable relay ramp between two west-dipping normal faults adds additional heterogeneity.
(3) Conjugate deformation features (faults and fractures) focus vertical movement of water downward and/or promote flow parallel to the intersection of structures and thus compartmentalize water between subvertical faults (causing significant lateral electrical resistivity and radar signal attenuation heterogeneity, with implications for moisture content heterogeneity).
(4) Small-scale deformation styles within matrix blocks are likely influenced by bed thickness, grain size, degree of clay alteration, glass and ash content, and sintering.
(5) Deformation styles suggest brittle deformation behavior at the bed scale but relatively ductile deformation behavior at the microscopic scale.
(6) Overprinting of vertical fractures with nonvertical fractures and conjugate-style faulting increases fracture permeability.
(7) Geometric mean gas permeabilities of a primary ash-fall deposit and a reworked tuffaceous deposit are not significantly different, but their identical arithmetic coefficients of variation indicate erratically large values attributable to the secondary permeability of open fractures.

Deformation features associated with subvertical faults increase the heterogeneity of hydrologic properties in the lateral direction relative to an undeformed protolith. Heterogeneities like these will reduce the lateral continuity of capillary or permeability barriers and thus limit any redistribution of percolation that would result from lateral flow diversion (Ho and Webb, 1998). In this study, we have shown that microstructural analysis reveals structurally induced porosity variations at the micrometer to millimeter scale, gas permeability data demonstrate the influence of deformation on intrinsic permeability at the centimeter to tens of centimeters scale, and geophysical data indicate lateral variations on the meter to tens of meters scale in subhorizontally bedded layers. Standard point measurement techniques spanning one or two orders of magnitude in averaging volume that are used to estimate hydrologic modeling parameters are not sufficient to address questions about the potential for lateral flow disruption by structural deformation features. An integrated, multiscale approach is best adapted to reveal the potential effects of structural overprinting on fluid flow. All together, our observations and data show heterogeneity over seven orders of magnitude of length scale. Structurally enhanced porosity and permeability heterogeneities (with $k$ spanning three orders of magnitude) will tend to limit the length scale of lateral flow diversion, redirect flow downward, and enhance vertical fluid movement within the vadose zone.

Detailed three-dimensional modeling of the nonwelded Paintbrush Tuff at the hundreds of meters scale—its lithologic properties, gradational contacts, slope interruptions and reversals, and small-displacement, fault-related deformation structures—would improve understanding of the potential length scale of lateral flow diversion within this hydrologic unit, the associated uncertainty, and the effects of this uncertainty. Small-displacement faults are known to cross all subunits of the nonwelded Paintbrush Tuff (e.g., Manepally et al., 2007). Although localized lateral flow along capillary or permeability barriers is likely associated with some subunits, the pervasive presence of secondary structural heterogeneities similar to those examined in this analog study suggests that lateral flow within the unit is unlikely over distances greater than the average small-displacement fault spacing in each subunit. At a minimum, small faults spaced on the order of tens of meters or less (Ofoegbu et al., 2001; Fedors et al., 2002; Manepally et al., 2007) should induce local changes in matrix properties that, in turn, induce vertical flow (Waiting et al., 2001; Dinwiddie et al., 2006).

## ACKNOWLEDGMENTS

The authors gratefully acknowledge field assistance provided by Donald R. Bannon and Richard Heermance. The Bishop Tablelands light detection and ranging (LiDAR) data (used to construct Fig. 1) is courtesy of Chevron® U.S.A. Inc., a Pennsylvania company, acting through its Chevron Energy Technology Company division.

We appreciate extensive discussions with Randall W. Fedors, Brittain E. Hill, James P. Evans, and Robert E. Grimm and the comments that three anonymous peer reviewers provided. We are also grateful to Ronald T. Green, Alan P. Morris, and Robert J. Lenhard for their technical reviews and to Gordon W. Wittmeyer and Randall W. Fedors for their programmatic reviews of this manuscript, each of which improved it greatly. This article describes work performed by the Center for Nuclear Waste Regulatory Analyses (CNWRA) and its contractors for the U.S. Nuclear Regulatory Commission (USNRC) under Contract NRC-02-07-006. The non-near-surface-geophysics activities reported here were performed on behalf of the USNRC Office of Nuclear Material Safety and Safeguards, Division of High-Level Waste Repository Safety. This article also describes near-surface geophysical field work performed by Southwest Research Institute on behalf of the National Aeronautics and Space Administration under Grant NNG05GM32G. This article is an independent product of the CNWRA and does not necessarily reflect the view or regulatory position of the USNRC.

## REFERENCES CITED

Antonellini, M., and Aydin, A., 1994, Effect of faulting on fluid flow in porous sandstones: Petrophysical properties: American Association of Petroleum Geologists (AAPG) Bulletin, v. 78, p. 355–377.

Balsillie, J.H., Donoghue, J.F., Butler, K.M., and Koch, J.L., 2002, Plotting equation for Gaussian percentiles and a spreadsheet program for generating probability plots: Journal of Sedimentary Research, v. 72, no. 6, p. 929–933, doi:10.1306/040402720929.

Barr, D.L., Moyer, T.C., Singleton, W.L., Albin, A.L., Lung, R.C., Lee, A.C., Beason, S.C., and Eatman, G.L.W., 1996, Geology of the North Ramp—Station 4+00 to 28+00, Exploratory Studies Facility, Yucca Mountain Project, Yucca Mountain, Nevada: Denver, Colorado, Bureau of Reclamation and U.S. Geological Survey, 265 p.

Bense, V.F., and Person, M.A., 2006, Faults as conduit-barrier systems to fluid flow in siliciclastic sedimentary aquifers: Water Resources Research, v. 42, doi:10.1029/2005WR004480.

Boggs, S., Jr., 1992, Petrology of Sedimentary Rocks: New York, Macmillan Publishing Co., 707 p.

Boggs, S., Jr., 1995, Principles of Sedimentology and Stratigraphy: Englewood Cliffs, New Jersey, Prentice-Hall Inc., 774 p.

Caine, J.S., Evans, J.P., and Forster, C.B., 1996, Fault zone architecture and permeability structure: Geology, v. 24, p. 1025–1028, doi:10.1130/0091-7613(1996)024<1025:FZAAPS>2.3.CO;2.

Cashman, S.M., and Cashman, K.V., 2000, Cataclasis and deformation band formation in unconsolidated marine terrace sand, Humboldt County, California: Geology, v. 28, no. 2, p. 111–114, doi:10.1130/0091-7613(2000)28<111:CADFIU>2.0.CO;2.

Cashman, S.M., Baldwin, J.N., Cashman, K.V., Swanson, K., and Crawford, R., 2007, Microstructures developed by coseismic and aseismic faulting in near-surface sediments, San Andreas fault, California: Geology, v. 35, no. 7, p. 611–614, doi:10.1130/G23545A.1.

Copeland, K., 2003, Fly Ash Properties and Uses: Italy, Texas, Monolithic Dome Institute: www.static.monolithic.com/construction/flyash/index.html (accessed 14 April 2011).

Dahan, O., Nativ, R., Adar, E.M., Berkowitz, B., and Ronen, Z., 1999, Field observation of flow in a fracture intersecting unsaturated chalk: Water Resources Research, v. 35, no. 11, p. 3315–3326, doi:10.1029/1999WR900198.

Dahan, O., Nativ, R., Adar, E.M., Berkowitz, B., and Weisbrod, N., 2000, On fracture structure and preferential flow in unsaturated chalk: Ground Water, v. 38, no. 3, p. 444–451, doi:10.1111/j.1745-6584.2000.tb00231.x.

Davis, S.N., 1969, Porosity and permeability in natural materials, *in* DeWiest, R.J.M., ed., Flow through Porous Media: New York, Academic Press, p. 53–89.

Dijk, P., and Berkowitz, B., 1998, Precipitation and dissolution of reactive solutes in fractures: Water Resources Research, v. 34, no. 3, p. 457–470, doi:10.1029/97WR03238.

Dinwiddie, C.L., 2005, The small-drillhole minipermeameter probe for in-situ permeability measurement: Society of Petroleum Engineers (SPE): Reservoir Evaluation & Engineering, v. 8, no. 6, p. 491–501.

Dinwiddie, C.L., Molz, F.J., III, and Castle, J.W., 2003, A new small drill hole minipermeameter probe for in situ permeability measurement: Fluid mechanics and geometrical factors: Water Resources Research, v. 39, no. 7, doi:10.1029/2001WR001179.

Dinwiddie, C.L., Bradbury, K.K., McGinnis, R.N., Fedors, R.W., and Ferrill, D.A., 2006, Fault zone deformation overprints permeability of nonwelded ignimbrite: Chalk Cove fault, Bishop Tuff, Bishop, California: Vadose Zone Journal, v. 5, p. 610–627, doi:10.2136/vzj2005.0062.

Dinwiddie, C.L., Chan, M.A., McGinnis, R.N., Myers, J.L., and Holliday, W.S., 2011, Chronicles of vadose zone diagenesis: Cone-shaped iron oxide concretions, Triassic Trujillo Formation, Palo Duro Canyon, Texas: Geofluids, p. 1–10, doi:10.1111/j.1468-8123.2010.00321.x.

Dragila, M.I., and Weisbrod, N., 2004, Fluid motion through an unsaturated fracture junction: Water Resources Research, v. 40, doi:10.1029/2003WR002588.

Dragila, M.I., and Wheatcraft, S.W., 2001, Free-surface films, *in* Conceptual Models of Flow and Transport in the Fractured Vadose Zone: Washington, D.C., U.S. National Committee for Rock Mechanics, Board on Earth Sciences and Resources, National Research Council, National Academies Press, p. 217–241.

Du Bernard, X., Eichhubl, P., and Aydin, A., 2002, Dilation bands: A new form of localized failure in granular material: Geophysical Research Letters, v. 29, no. 24, p. 1–4, doi:10.1029/2002GL015966.

Eatman, G.L.W., Singleton, W.L., Moyer, T.C., Barr, D.L., Albin, A.L., Lung, R.C., and Beason, S.C., 1997, Geology of the South Ramp–Station 55+00 to 78+77, Exploratory Studies Facility, Yucca Mountain Project, Yucca Mountain, Nevada: Denver, Colorado, Bureau of Reclamation and U.S. Geological Survey, 279 p.

Eliassi, M., and Glass, R.J., 2002, On the porous-continuum modeling of gravity-driven fingers in unsaturated materials: Extension of standard theory with a hold-back-pile-up effect: Water Resources Research, v. 38, no. 11, doi:10.1029/2001WR001131.

Engstrom, D.A., and Rautman, C.A., 1996, Geology of the USW SD-9 Drill Hole, Yucca Mountain, Nevada: Albuquerque, New Mexico, Sandia National Laboratories Report SAND96-2030, 128 p.

Evans, J.P., and Bradbury, K.K., 2004, Faulting and fracturing of nonwelded Bishop Tuff, eastern California: Deformation mechanisms in very porous materials in the vadose zone: Vadose Zone Journal, v. 3, p. 602–623, doi:10.2113/3.2.602.

Evans, J.P., and Bradbury, K.K., 2007, Fractured dirt: Deformation textures and processes in sediment and other unconsolidated deposits: Geology, v. 35, no. 7, p. 671–672, doi:10.1130/Focus072007.1.

Fabryka-Martin, J.T., Flint, A.L., Flint, L.E., Wolfsberg, A.V., Sweetkind, D.S., Hudson, D., Roach, J.L., Winters, S.T., Wolfsberg, L.E., and Bridges, J.A., 1998a, Using chloride to trace water movement in the unsaturated zone at Yucca Mountain, *in* Proceedings of the 8th International Conference on High-Level Radioactive Waste Management: La Grange Park, Illinois, American Nuclear Society, p. 264–267.

Fabryka-Martin, J.T., Wolfsberg, A.V., Levy, S.S., Roach, J.L., Winters, S.T., Wolfsberg, L.E., Elmore, D., and Sharma, P., 1998b, Distribution of fast hydrologic paths in the unsaturated zone at Yucca Mountain, *in* Proceedings of the 8th International Conference on High-Level Radioactive Waste Management: La Grange Park, Illinois, American Nuclear Society, p. 93–96.

Fedors, R.W., Winterle, J.R., Illman, W.A., Dinwiddie, C.L., and Hughson, D.L., 2002, Unsaturated zone flow at Yucca Mountain, Nevada: Effects of fracture heterogeneity and flow in the nonwelded Paintbrush Tuff unit: San Antonio, Texas, Center for Nuclear Waste Regulatory Analyses: www.nrc.gov/reading-rm/adams.html#web-based-adams, accession no. ML022460157 (accessed 14 April 2011).

Ferrill, D.A., and Morris, A.P., 2001, Displacement gradient and deformation in normal fault systems: Journal of Structural Geology, v. 23, p. 619–638, doi:10.1016/S0191-8141(00)00139-5.

Ferrill, D.A., Stamatakos, J.A., and Sims, D., 1999, Normal fault corrugation: Implications for growth and seismicity of active normal faults: Journal of Structural Geology, v. 21, p. 1027–1038, doi:10.1016/S0191-8141(99)00017-6.

Ferrill, D.A., Morris, A., Stamatakos, J.A., and Sims, D., 2000, Crossing conjugate normal faults: American Association of Petroleum Geologists (AAPG) Bulletin, v. 84, no. 10, p. 1543–1559.

Ferrill, D.A., Morris, A.P., Sims, D.W., Waiting, D.J., and Hasegawa, S., 2005, Development of synthetic layer dip adjacent to normal faults, *in* Sorkhabi, R., and Tsuji, Y., eds., Faults, Fluid Flow, and Petroleum Traps: American Association of Petroleum Geologists Memoir 85, p. 125–138.

Ferrill, D.A., Morris, A.P., and McGinnis, R.N., 2009, Crossing conjugate normal faults in field exposures and seismic data: American Association of Petroleum Geologists (AAPG) Bulletin, v. 93, no. 11, p. 1471–1488, doi:10.1306/06250909039.

Fetter, C.W., 1994, Applied Hydrogeology: New York, Macmillan College Publishing Company, 691 p.

Fisher, R., 1961, Proposed classification of volcaniclastic sediments and rocks: Geological Society of America Bulletin, v. 72, p. 1409–1414, doi:10.1130/0016-7606(1961)72[1409:PCOVSA]2.0.CO;2.

Fisher, R., 1966, Rocks composed of volcanic fragments and their classification: Earth-Science Reviews, v. 1, p. 287–298, doi:10.1016/0012-8252(66)90010-9.

Flint, A.L., Flint, L.E., Kwicklis, E.M., Bodvarsson, G.S., and Fabryka-Martin, J., 2001, Hydrology of Yucca Mountain, Nevada: Reviews of Geophysics, v. 39, no. 4, p. 447–470, doi:10.1029/1999RG000075.

Flint, L.E., and Selker, J.S., 2003, Use of porosity to estimate hydraulic properties of volcanic tuffs: Advances in Water Resources, v. 26, p. 561–571, doi:10.1016/S0309-1708(02)00182-3.

Flint, L.E., Flint, A.L., and Selker, J.S., 2003, Influence of transitional volcanic strata on lateral diversion at Yucca Mountain, Nevada: Water Resources Research, v. 39, no. 4, doi:10.1029/2002WR001503.

Fossen, H., Schultz, R.A., Shipton, Z.K., and Mair, K., 2007, Deformation bands in sandstone: A review: Journal of the Geological Society of London, v. 164, p. 755–769, doi:10.1144/0016-76492006-036.

Freifeld, B.M., and Oldenburg, C.M., 2000, Restricted interval Guelph permeameter: Theory and application: Water Resources Research, v. 36, no. 6, p. 1373–1380, doi:10.1029/2000WR900034.

Ghezzehei, T.A., 2004, Constraints for flow regimes on smooth fracture surfaces: Water Resources Research, v. 40, doi:10.1029/2004WR003164.

Ghezzehei, T.A., and Or, D., 2005, Liquid fragmentation and intermittent flow regimes in unsaturated fractured media: Water Resources Research, v. 41, doi:10.1029/2004WR003834.

Glass, R.J., and Nicholl, M.J., 1996, Physics of gravity fingering of immiscible fluids within porous media: An overview of current understanding and selected complicating factors: Geoderma, v. 70, p. 133–163, doi:10.1016/0016-7061(95)00078-X.

Glass, R.J., Steenhuis, T.S., and Parlange, J.-Y., 1988, Wetting front instability as a rapid and far-reaching hydrologic process in the vadose zone: Journal of Contaminant Hydrology, v. 3, p. 207–226, doi:10.1016/0169-7722(88)90032-0.

Glass, R.J., Parlange, J.-Y., and Steenhuis, T., 1989a, Wetting front instability: 1. Theoretical discussion and dimensional analysis: Water Resources Research, v. 25, no. 6, p. 1187–1194, doi:10.1029/WR025i006p01187.

Glass, R.J., Steenhuis, T., and Parlange, J.-Y., 1989b, Wetting front instability: 2. Experimental determination of relationships between system parameters and two-dimensional unstable flow field behavior in initially dry porous media: Water Resources Research, v. 25, no. 6, p. 1195–1207, doi:10.1029/WR025i006p01195.

Glass, R.J., Nicholl, M.J., and Tidwell, V.C., 1995, Challenging models for flow in unsaturated, fractured rock through exploration of small scale processes: Geophysical Research Letters, v. 22, no. 11, p. 1457–1460, doi:10.1029/95GL01490.

Glass, R.J., Nicholl, M.J., Pringle, S.E., and Wood, T.R., 2002, Unsaturated flow through a fracture-matrix network: Dynamic preferential pathways in mesoscale laboratory experiments: Water Resources Research, v. 38, no. 12, doi:10.1029/2001WR001002.

Glass, R.J., Nicholl, M.J., Rajaram, H., and Wood, T.R., 2003, Unsaturated flow through fracture networks: Evolution of liquid phase structure, dynamics, and the critical importance of fracture intersections: Water Resources Research, v. 39, no. 12, doi:10.1029/2003WR002015.

Heynekamp, M.R., Goodwin, L.B., Mozley, P.S., and Haneburg, W.C., 1999, Controls on fault-zone architectures in poorly lithified sediments, Rio Grande Rift, New Mexico: Implications for fault-zone permeability and fluid flow, *in* Haneberg, W.C., Mozley, P.S., Moore, J.C., and Goodwin, L.B., eds., Faults and Subsurface Fluid Flow in the Shallow Crust: American Geophysical Union Geophysical Monograph 113, p. 27–49.

Hildreth, W., 1979, The Bishop Tuff: Evidence for the origin of compositional zonation in silicic magma chambers, *in* Chapin, C.E., and Elston, W.E., eds., Ashflow Tuffs: Geological Society of America Special Paper 180, p. 43–75.

Hill, D.E., and Parlange, J.-Y., 1972, Wetting front instability in layered soils: Soil Science Society of America Proceedings, v. 36, p. 697–702, doi:10.2136/sssaj1972.0361 5995003600050010x.

Ho, C.K., and Webb, S.W., 1998, Capillary barrier performance in heterogeneous porous media: Water Resources Research, v. 34, no. 4, p. 603–609, doi:10.1029/98WR00217.

Illman, W.A., and Hughson, D.L., 2005, Stochastic simulations of steady state unsaturated flow in a three-layer, heterogeneous, dual continuum model of fractured rock: Journal of Hydrology (Amsterdam), v. 307, p. 17–37, doi:10.1016/j.jhydrol.2004.09.015.

Istok, J.D., Rautman, C.A., Flint, L.E., and Flint, A.L., 1994, Spatial variability in hydrologic properties of a volcanic tuff: Ground Water, v. 32, no. 5, p. 751–760, doi:10.1111/j.1745-6584.1994.tb00916.x.

Izett, G.A., 1981, Volcanic ash beds; recorders of upper Cenozoic silicic pyroclastic volcanism in the western United States: Journal of Geophysical Research, v. 86, no. B11, p. 10,200–10,222, doi:10.1029/JB086iB11p10200.

Izett, G.A., Obradovich, J.D., and Mehnert, H.H., 1988, The Bishop Ash Bed and Some Older Chemically and Mineralogically Similar Ash Beds in California, Nevada, and Utah: U.S. Geological Survey Bulletin 1675, 37 p.

Johansen, T.E.S., Fossen, H., and Kluge, R., 2005, The impact of syn-faulting porosity reduction on damage zone architecture in porous sandstone: An outcrop example from the Moab fault, Utah: Journal of Structural Geology, v. 27, p. 1469–1485, doi:10.1016/j.jsg.2005.01.014.

Kwicklis, E.M., Thamir, F., Healy, R.W., and Hampson, D., 1998, Numerical Simulation of Air- and Water-Flow Experiments in a Block of Variably Saturated, Fractured Tuff from Yucca Mountain, Nevada: U.S. Geological Survey Water Resources Investigations Report 97-4274, 64 p.

Liu, H.H., Doughty, C., and Bodvarsson, G.S., 1998, An active fracture model for unsaturated flow and transport in fractured rocks: Water Resources Research, v. 34, p. 2633–2646, doi:10.1029/98WR02040.

Loke, M.H., 2010, Manual for RES2DINV ver. 3.59: Malaysia Geotomo Software, 151 p.

Loke, M.H., and Barker, R.D., 1996, Rapid least-square inversion of apparent resistivity pseudosections by a quasi-Newton method: Geophysical Prospecting, v. 44, p. 131–152, doi:10.1111/j.1365-2478.1996.tb00142.x.

Main, I.G., Mair, K., Kwon, O., Elphick, S.C., and Ngwenya, B.T., 2001, Experimental constraints on the mechanical and hydraulic properties of deformation bands, in porous sandstones: A review, *in* Holdsworth, R.E., et al., eds., The Nature and Significance of Fault Zone Weakening: Geological Society of London Special Publication 186, p. 43–63.

Manepally, C., Bradbury, K., Colton, S., Dinwiddie, C., Green, R., McGinnis, R., Sims, D., Smart, K., and Walter, G., 2007, The Nature of Flow in the Faulted and Fractured Paintbrush Nonwelded Hydrogeologic Unit: San Antonio, Texas, Center for Nuclear Waste Regulatory Analyses: www.nrc.gov/reading-rm/adams.html#web-based-adams, using accession no. ML071410138 (accessed 14 April 2011).

McGinnis, R.N., Morris, A.P., Ferrill, D.A., and Dinwiddie, C.L., 2009, Deformation analysis of tuffaceous sediments in the Volcanic Tableland near Bishop, California: Lithosphere, v. 1, no. 5, p. 291–304, doi:10.1130/L43.1.

Metz, J., and Mahood, G.A., 1985, Precursors to the Bishop Tuff eruption: Glass Mountain, Long Valley, California: Journal of Geophysical Research, v. 90, p. 11,121–11,126.

Molz, F.J., III, Dinwiddie, C.L., and Wilson, J.L., 2003, A physical basis for calculating instrument spatial weighting functions in homogeneous systems: Water Resources Research, v. 39, no. 4, doi:10.1029/2001WR001220.

Muhunthan, B., Taha, R., and Said, J., 2004, Geotechnical engineering properties of incinerator ash mixes: Journal of the Air & Waste Management Association, v. 54, no. 8, p. 985–991.

Odling, N.E., Harris, S.D., and Knipe, R.J., 2004, Permeability scaling properties of fault damage zones in siliciclastic rocks: Journal of Structural Geology, v. 26, p. 1727–1747, doi:10.1016/j.jsg.2004.02.005.

Ofoegbu, G.I., Painter, S., Chen, R., Fedors, R.W., and Ferrill, D.A., 2001, Geomechanical and thermal effects on moisture flow at the proposed Yucca Mountain nuclear waste repository: Nuclear Technology, v. 134, no. 3, p. 241–262.

Oldenburg, C.M., and Pruess, K., 1993, On numerical modeling of capillary barriers: Water Resources Research, v. 29, no. 4, p. 1045–1056, doi:10.1029/92WR02875.

Pan, L., Wu, Y.-S., and Zhang, K., 2004, A modeling study of flow diversion and focusing in unsaturated fractured rocks: Vadose Zone Journal, v. 3, p. 233–246.

Parkhomenko, E.I., 1971, Electrification Phenomena in Rocks (translation by G.V. Keller): New York, Plenum Press, 285 p.

Persoff, P., and Pruess, K., 1993, Flow visualization and relative permeability measurement in rough-walled fractures, *in* Proceedings of 4th International High Level Radioactive Waste Management Conference: La Grange Park, Illinois, American Nuclear Society, p. 2033–2041.

Pinter, N., Keller, E.A., and West, R.B., 1994, Relative dating of terraces of the Owens River, northern Owens Valley, California, and correlation with moraines of the Sierra Nevada: Quaternary Research, v. 42, p. 266–276, doi:10.1006/qres.1994.1077.

Pruess, K., 1998, On water seepage and fast preferential flow in heterogeneous, unsaturated rock fractures: Journal of Contaminant Hydrology, v. 30, p. 333–362, doi:10.1016/S0169-7722(97)00049-1.

Pruess, K., 1999, A mechanistic model for water seepage through thick unsaturated zones in fractured rocks of low matrix permeability: Water Resources Research, v. 35, no. 4, p. 1039–1051, doi:10.1029/1998WR900100.

Pruess, K., 2001, Two-phase unsaturated flow at Yucca Mountain, Nevada: A report on current understanding, *in* Evans, D.D., Nicholson, T.J., and Rasmussen, T.C., eds., Flow and Transport through Unsaturated Fractured Rock, 2nd ed.: American Geophysical Union Geophysical Monograph 42, p. 113–133.

Pruess, K., and Tsang, Y.W., 1990, On two-phase relative permeability and capillary pressure of rough-walled rock fractures: Water Resources Research, v. 26, no. 9, p. 1915–1926, doi:10.1029/WR026i009p01915.

Rautman, C.A., and Engstrom, D.A., 1996a, Geology of the USW SD-7 Drill Hole, Yucca Mountain, Nevada: Albuquerque, New Mexico, Sandia National Laboratories Report SAND96-1474, 164 p.

Rautman, C.A., and Engstrom, D.A., 1996b, Geology of the USW SD-12 Drill Hole, Yucca Mountain, Nevada: Albuquerque, New Mexico, Sandia National Laboratories Report SAND96-1368, 132 p.

Rautman, C.A., Flint, L.E., Flint, A.L., and Istok, J.D., 1995, Physical and Hydrologic Properties of Outcrop Samples from a Nonwelded to Welded Tuff Transition, Yucca Mountain, Nevada: U.S. Geological Survey Water-Resources Investigations Report 95-4061, 28 p.

Rawling, G., and Goodwin, L., 2003, Cataclasis and particulate flow in faulted, poorly lithified sediments: Journal of Structural Geology, v. 25, p. 317–331, doi:10.1016/S0191-8141(02)00041-X.

Roberts, J.J., 2002, Electrical properties of microporous rock as a function of saturation and temperature: Journal of Applied Physics, v. 91, no. 3, p. 1687–1694, doi:10.1063/1.1430544.

Roberts, J.J., and Lin, W., 1997, Electrical properties of partially saturated Topopah Spring tuff: Water distribution as a function of saturation: Water Resources Research, v. 33, no. 4, p. 577–587, doi:10.1029/96WR03905.

Ross, B., 1990, The diversion capacity of capillary barriers: Water Resources Research, v. 26, no. 10, p. 2625–2629, doi:10.1029/WR026i010p02625.

Salve, R., and Oldenburg, C.M., 2001, Water flow within a fault in altered nonwelded tuff: Water Resources Research, v. 37, no. 12, p. 3043–3056, doi:10.1029/2001WR000322.

Salve, R., Oldenburg, C.M., and Wang, J.S.Y., 2003, Fault-matrix interactions in nonwelded tuff of the Paintbrush Group at Yucca Mountain: Journal of Contaminant Hydrology, v. 62/63, p. 269–286, doi:10.1016/S0169-7722(02)00165-1.

Sarna-Wojcicki, A.M., Bowman, H.R., Meyer, C.E., Russell, P.C., Woodward, M.J., McCoy, G., Rowe, J.J., Jr., Baedecker, P.A., Asaro, F., and Michael, H., 1984, Chemical analyses, correlations, and ages of Upper Pliocene and Pleistocene ash layers of east-central and southern California: U.S. Geological Survey Professional Paper 1293, 40 p.

Sarna-Wojcicki, A.M., Pringle, M.S., and Wijbrans, J., 2000, New $^{39}Ar/^{40}Ar$ age of the Bishop Tuff from multiple sites and sediment rate calibration for the Matuyama–Bruhnes boundary: Journal of Geophysical Research, v. 105, no. B9, p. 21,431–21,443.

Schleicher, A.M., van der Pluijm, B.A., Solum, J.G., and Warr, L.N., 2006, Origin and significance of clay-coated fractures in mudrock fragments of the SAFOD borehole (Parkfield, California): Geophysical Research Letters, v. 33, doi:10.1029/2006GL026505.

Schleicher, A.M., Tourscher, S.N., van der Pluijm, B.A., and Warr, L.N., 2009, Constraints on mineralization, fluid-rock interaction, and mass transfer during faulting at 2–3 km depth from the SAFOD drill hole: Journal of Geophysical Research, v. 114, doi:10.1029/2008JB006092.

Schleicher, A.M., van der Pluijm, B.A., and Warr, L.N., 2010, Nanocoatings of clay and creep of the San Andreas fault at Parkfield, California: Geology, v. 38, no. 7, p. 667–670, doi:10.1130/G31091.1.

Schmid, R., 1981, Descriptive nomenclature and classification of pyroclastic deposits and fragments: Recommendations of the IUGS Subcommission on the Systematics of Igneous Rocks: Geology, v. 9, no. 1, p. 41–43, doi:10.1130/0091-7613(1981)9<41:DNACOP>2.0.CO;2.

Sigda, J.M., and Wilson, J.L., 2003, Are faults preferential flow paths through semiarid and arid vadose zones?: Water Resources Research, v. 39, no. 8, doi:10.1029/2002WR001406.

Sigda, J.M., Goodwin, L.B., Mozley, P.S., and Wilson, J.L., 1999, Permeability alteration in small-displacement faults in poorly lithified sediments: Rio Grande rift, central New Mexico, *in* Haneberg, W.C., et al., ed., Faults and Subsurface Fluid Flow in the Shallow Crust: American Geophysical Union Geophysical Monograph 113, p. 51–68.

Smith, G.A., 1986, Coarse-grained nonmarine volcaniclastic sediment: Terminology and depositional process: Geological Society of America Bulletin, v. 97, p. 1–10, doi:10.1130/0016-7606(1986)97<1:CNVSTA>2.0.CO;2.

Stillman, D., and Olhoeft, G., 2008, Frequency and temperature dependence in electromagnetic properties of Martian analog minerals: Journal of Geophysical Research, v. 113, E09005, doi:10.1029/2007JE002977.

Su, G.W., Geller, J.T., Pruess, K., and Wen, F., 1999, Experimental studies of water seepage and intermittent flow in unsaturated, rough-walled fractures: Water Resources Research, v. 35, no. 4, p. 1019–1037, doi:10.1029/1998WR900127.

Sweetkind, D.S., Verbeek, E.R., Geslin, J.K., and Moyer, T.C., 1995, Fracture Character of the Paintbrush Tuff Nonwelded Hydrologic Unit, Yucca Mountain, Nevada:

Denver, Colorado, U.S. Geological Survey Administrative Report, 202 p.

Tokunaga, T.K., and Wan, J., 1997, Water film flow along fracture surfaces of porous rock: Water Resources Research, v. 33, no. 6, p. 1287–1295, doi:10.1029/97WR00473.

Tokunaga, T.K., Wan, J., and Sutton, S.R., 2000, Transient film flow on rough fracture surfaces: Water Resources Research, v. 36, no. 7, p. 1737–1746, doi:10.1029/2000WR900079.

Vaniman, D.T., Chipera, S.J., Bish, D.L., Carey, J.W., and Levy, S.S., 2001, Quantification of unsaturated-zone alteration and cation exchange in zeolitized tuffs at Yucca Mountain, Nevada, USA: Geochimica et Cosmochimica Acta, v. 65, no. 20, p. 3409–3433, doi:10.1016/S0016-7037(01)00682-2.

Waiting, D.J., Chen, R., Crider, J.G., Dunne, W.M., Fedors, R.W., Ferrill, D.A., Gray, M.B., Hill, B.E., LaFemina, P.C., McKague, H.L., Morris, A.P., Sims, D.W., and Stamatakos, J.A., 2001, Technical Assessment of Structural Deformation and Seismicity at Yucca Mountain, Nevada: San Antonio, Texas, Center for Nuclear Waste Regulatory Analyses, U.S. NRC Contract NRC-02–97–009: www.nrc.gov/reading-rm/adams.html#web-based-adams, using accession no. ML033630629 (accessed 27 May 2011).

Webb, S.W., 1997, Generalization of Ross' tilted capillary barrier diversion formula for different two-phase characteristic curves: Water Resources Research, v. 33, no. 8, p. 1855–1859, doi:10.1029/97WR01231.

Western Regional Climate Center, 2011, Bishop WSO (Weather Service Office) Airport, California, Monthly Total Precipitation: http://www.wrcc.dri.edu/cgi-bin/cliMAIN.pl?ca0822 (accessed 8 November 2011).

Wilson, C.J.N., and Hildreth, W., 1998, Hybrid fall deposits in the Bishop Tuff, California: A novel pyroclastic depositional mechanism: Geology, v. 26, no. 1, p. 7–10, doi:10.1130/0091-7613(1998)026<0007:HFDITB>2.3.CO;2.

Wilson, J.E., Goodwin, L.B., and Lewis, C.J., 2003, Deformation bands in nonwelded ignimbrites: Petrophysical controls on fault-zone deformation and evidence of preferential fluid flow: Geology, v. 31, no. 10, p. 837–840, doi:10.1130/G19667R.1.

Wilson, M.L., 1996, Lateral diversion in the PTn unit: Capillary barrier analysis, *in* Proceedings of the 7th International High Level Radioactive Waste Management Conference: La Grange Park, Illinois, American Nuclear Society, p. 111–113.

Wolf, H., 2003, Experimental investigation of shear band patterns in granular material: Journal of Structural Geology, v. 25, no. 8, p. 1229–1240, doi:10.1016/S0191-8141(02)00163-3.

Wu, Y.-S., Zhang, W., Pan, L., Hinds, J., and Bodvarsson, G.S., 2002, Modeling capillary barriers in unsaturated fractured rock: Water Resources Research, v. 38, no. 11, doi:10.1029/2001WR000852.

Yielding, G., Freeman, B., and Needham, D.T., 1997, Quantitative fault seal prediction: American Association of Petroleum Geologists (AAPG) Bulletin, v. 81, no. 6, p. 897–917.

MANUSCRIPT RECEIVED 21 SEPTEMBER 2011
MANUSCRIPT ACCEPTED 28 OCTOBER 2011

Printed in the USA